From network pharmacology to experimental verification: *Angelica sinensis* and its key constituent β-sitosterol exert anti-liver cancer effects through the p53 signaling pathway

YING DU[1*], YANG SONG[1*], YUTING FAN[2*], WEITONG LI[1], YUXIN ZHANG[1], HAOTIAN SHEN[1], BIN TANG[3], JINHUI WANG[4], FENGMEI DENG[1] and LI CHENG[1]

[1]College of Basic Medical Sciences, Chengdu Medical College, Chengdu, Sichuan 610500, P.R. China; [2]College of Laboratory Medicine, Chengdu Medical College, Chengdu, Sichuan 610500, P.R. China; [3]Department of Ultrasound Medicine, The First Affiliated Hospital of Chengdu Medical College, Chengdu, Sichuan 610500, P.R. China; [4]School of Pharmacy, Harbin Medical University, Harbin, Heilongjiang 150081, P.R. China

Received March 27, 2026; Accepted October 16, 2026

DOI: 10.3892/mmr.2026.14079

Abstract. Liver cancer remains a major cause of cancer mortality and the limited benefit of existing therapies leaves a clear need for new therapeutic agents. Although *Angelica sinensis* (AS) shows broad antitumor potential, its mechanistic basis against liver cancer remains unclear. The present study revealed that AS reduced the viability, proliferation and migration of the HepG2 human liver cancer cell line. Network pharmacology p2ointed to several putative targets including insulin, peroxisome proliferator-activated receptor γ, nuclear factor κB subunit 1, estrogen receptor 1 and albumin. By combining molecular docking, molecular dynamics simulation and Cell Counting Kit-8 cell viability screening, β-sitosterol (BS) was identified from the candidate compounds of AS for further study, based on its stable interactions with central targets and its strong antiproliferative activity against HepG2 cells *in vitro*. Mechanistic assays of BS revealed that its anti-liver cancer effect was mediated through the p53 pathway. BS treatment increased the proportion of apoptotic cells, together with increased expression of the tumor suppressor protein p53 and the pro-apoptotic proteins Bax and Caspase-3, and reduced expression of the anti-apoptotic protein Bcl-2. Co-treatment with pifithrin-α hydrobromide, a p53 inhibitor, partly reduced the proportion of apoptotic cells and partly reversed these changes in protein expression, confirming a p53-dependent mechanism. The present study clarified the mechanisms by which AS, and its active component BS, suppress the proliferation and migration of liver cancer cells and trigger apoptosis through the modulation of the p53 pathway. These results support AS and BS as promising leads for development of plant-derived therapies against liver cancer.

Correspondence to: Professor Fengmei Deng or Professor Li Cheng, College of Basic Medical Sciences, Chengdu Medical College, 783 Xindu Avenue, Xindu, Chengdu, Sichuan 610500, P.R. China
E-mail: dengfm2004@163.com
E-mail: 852649464@qq.com

*Contributed equally

Key words: liver cancer, *Angelica sinensis*, β-sitosterol, p53 signaling pathway, apoptosis

Introduction

Primary liver cancer is a major global health burden, with its incidence and mortality ranking sixth and third, respectively, among common malignancies worldwide (1-4). Liver cancer is commonly preceded and driven by chronic liver injury, with major risk factors including hepatotropic virus infection, azoholic cirrhosis and metabolic dysfunction-associated steatotic liver disease (5). Current treatment strategies for liver cancer include liver resection, chemotherapy, immunotherapy, liver transplantation and newer targeted therapies (6). Because diagnosis is often delayed, a substantial proportion of liver cancer cases worldwide are diagnosed at locally advanced or metastatic disease, which means that a number of patients miss the best window for curative resection. Furthermore, frequent postoperative recurrence and poor surgical tolerance further limit treatment (7). Conventional chemotherapy is also limited by drug resistance, severe adverse effects and substantial economic pressure (8). These clinical challenges underscore the need for new therapeutic agents that are both safe and effective, while also highlighting the important clinical relevance of developing improved treatment strategies for liver cancer.

Over the past decade, traditional Chinese medicine (TCM) has been widely studied, particularly in China, and its clinical value has been discussed in disease prevention and treatment. This interest largely reflects its multitarget and multipathway synergistic effects as well as generally favorable safety. Consequently, TCM has been gradually incorporated into relevant clinical guidelines (9). However, current TCM research

still mainly focuses on the overall efficacy of compound decoctions, often lacking quantitative analysis and clear mechanistic explanation of individual medicinal constituents, particularly their defined active components. This lack of information on specific compounds and their molecular basis has emerged as a major bottleneck in the modernization and translation of TCM into clinical practice (10).

Angelica sinensis (AS), a widely used herb in TCM practice, contains active constituents such as volatile oils, polysaccharides and phytosterols. It has been reported to show several pharmacological effects, including hematopoietic, anti-inflammatory, antitumor, hepatorenal-protective and immunomodulatory effects (11). For example: i) Volatile oil components (such as ligustilide) are linked to antispasmodic, analgesic and anti-inflammatory actions (12); ii) angelica polysaccharides enhance proliferation and differentiation of bone marrow hematopoietic stem cells, modulate immune function and show antioxidant activity (13); and iii) phytosterols such as β-sitosterol (BS), can regulate lipid metabolism and exert immunoregulatory and antitumor effects, including inhibition of the proliferation of colon, breast and cervical cancer cells (14). Notably, although AS has accumulated supporting evidence in the management of cardiovascular and digestive disorders, and has shown potential in hepatoprotection and anti-fibrosis (15,16), its specific mechanisms against liver cancer need further clarification.

Against this backdrop, the present study employed an integrated strategy that combined computational analyses, including network pharmacology, molecular docking and molecular dynamics (MD) simulations, with cell-based assays to examine the anti-liver cancer potential and possible mechanisms of AS and its active component BS. In short, by adopting this framework of 'computational prediction and experimental validation', the present study aimed to generate experimental evidence for elucidating the active material basis and multitarget mechanisms of AS against liver cancer, and sought to support the identification and development of novel anti-liver cancer drug candidates from natural products.

Materials and methods

Chemicals and biological reagents. AS (purity 98%) was purchased from Shaanxi Sinuote Bio-Tech Co., Ltd. (cas. no. 4431-01-0). Stigmasterol (ST; purity 98.48%) was sourced from MedChemExpress (cat. no. HY-N0131), dissolved in acetone via ultrasonication (40 kHz, 25˚C, 10 min) to prepare a 2 mg/ml solution, and stored protected from light at -20˚C. BS (purity >98%) was purchased from MedChemExpress (cat. no. HY-N0171A), solubilized in 1 ml of anhydrous ethanol to prepare a 5 mg/ml stock solution, and stored protected from light at -20˚C. Pifithrin-α hydrobromide (PFT-α, a p53 inhibitor) was purchased from MedChemExpress (cat. no. HY-15484), dissolved in DMSO to prepare a 20 μM stock solution, followed by light-shielded storage at -80˚C. All antibodies were purchased from Proteintech Group Inc., including:Bcl-2 (cat. no. 26593-1-AP), cleaved Caspase-3 (cat. no. 25128-1-AP), Bax (cat. no. 50599-2-Ig), Caspase-3 (cat. no. 19677-1-AP), p53 (cat. no. 60283-2-Ig), MMP2 (cat. no. 10373-2-AP), MMP9 (cat. no. 10375-2-AP), GAPDH (cat. no. 60004-1-Ig) and β-Tubulin (cat. no. 66240-1-Ig).

Cell culture. The human liver cancer cell line HepG2 was purchased from Haixing Bioscience Co., Ltd. (cat. no. TCH-C196). Cells were routinely maintained in a humidified incubator at 37˚C with 5% CO_2. The culture medium was DMEM (cat. no. 10-013-CM; Corning, Inc.), supplemented as described with 10% FBS (cat. no. 35-081-CV; Corning, Inc.) and 1% penicillin-streptomycin. The cell line was authenticated via STR profiling.

Network pharmacology

Target acquisition. Liver cancer-related targets were retrieved by searching the GeneCards (https://www.genecards.org/), DisGeNET (https://www.disgenet.org/) and Comparative Toxicogenomics Database (https://ctdbase.org/) using 'liver cancer' as the keyword. Targets associated with AS and BS were collected by querying the Encyclopedia of TCM (http://www.tcmip.cn/ETCM/), High-Throughput Experiment- and Reference-Guided Database of TCM (HERB, http://herb.ac.cn/), and TCM systems pharmacology database and analysis platform (TCMSP, https://old.tcmsp-e.com/tcmsp.php), with the keywords '*Angelica sinensis*' and 'beta-sitosterol', respectively. Inclusion criteria included: i) Human protein-coding gene targets; and ii) gene-disease or gene-compound associations supported by experimental or manually curated evidence. Exclusion criteria included: i) non-human targets; ii) non-protein-coding genes; and iii) duplicate targets.

Identification of intersection targets. The online tool Venny 2.0 (https://bioinfogp.cnb.csic.es/tools/venny/index2.0.2.html) was employed to analyze set relationships. The respective target sets were imported into two separate lists within the software to generate a Venn diagram, from which the overlapping targets (common targets) were identified.

Construction of the protein-protein interaction (PPI) network. For PPI network construction, interactions were retrieved from the Search Tool for the Retrieval of Interacting Genes/Proteins (STRING) database (https://string-db.org/) with the species parameter set to 'Homo sapiens'. Network visualization and subsequent analysis were performed using Cytoscape (version 3.10.0; https://cytoscape.org/).

Screening of core targets. The CytoNCA plugin (version 2.1.6, https://apps.cytoscape.org/apps/CytoNCA) in Cytoscape (v3.10.0) was utilized for topological analysis aimed at identifying the core targets. Key features analyzed included degree, closeness centrality (CC), betweenness centrality (BC) and eigenvector centrality (EC), along with network centrality (NC) and local average connectivity (LAC) scores, which informed the preliminary screening.

Gene ontology (GO) and kyoto encyclopedia of genes and genomes (KEGG) enrichment analysis. The intersection targets were submitted to the Database for Annotation, Visualization, and Integrated Discovery (https://davidbioinformatics.nih.gov/) for GO functional enrichment analysis (https://geneontology.org/) and KEGG pathway enrichment analysis (https://www.kegg.jp/). Analysis was configured with the species restricted to Homo sapiens, a significance threshold of $P<0.01$ and the gene identifier defined as 'OFFICIAL_GENE_SYMBOL'.

Construction of the drug-disease-target-pathway integrated network. An integrated BS-liver cancer-target-pathway network was constructed and visualized using Cytoscape

(v3.10.0) to illustrate the interaction relationships among the compound, disease, target proteins and pathways.

Molecular docking. The three-dimensional (3D) molecular structures of BS (MOL000358) and ST (MOL000359), in mol2 format, were first downloaded from the TCMSP database (17). Concurrently, the crystal structures of the target proteins; insulin (INS), peroxisome proliferator-activated receptor g (PPARG), nuclear factor kB subunit 1 (NFKB1), estrogen receptor 1 (ESR1) and albumin (ALB), were downloaded from the RCSB Protein Data Bank (PDB; https://www.rcsb.org/). The obtained protein structures underwent preparation, which entailed the addition of hydrogen atoms and the elimination of water molecules, and were subsequently saved in PDB format. Finally, molecular docking calculations between the ligands and each target protein were performed using AutoDock software (version 4.2.6; https://autodock.scripps.edu/), and the results were visualized with PyMOL (version 2.6.0; https://pymol.org/).

MD simulation. MD simulations were executed using the Gromacs 2022.3 (https://manual.gromacs.org/2022.3/) software package. The small-molecule ligands were prepared using AmberTools22 (https://ambermd.org/), wherein the generalized AMBER force field parameters were assigned, and hydrogen atoms were added followed by Restrained Electrostatic Potential charge calculations using Gaussian 16W (Rev. C.01; https://gaussian.com/). Following charge assignment, the generated data assemblies were embedded into the system topology files. Subsequent simulations maintained constant conditions of 300 K and 1 bar. The systems were modeled using the Amber99sb-ildn force field, solvated with the Transferable Intermolecular Potential 3-Point water model, and neutralized by the addition of Na^+ ions. The simulation protocol comprised three consecutive phases. Each system was first subjected to energy minimization, followed by equilibration under the NVT ensemble (100 ps, $1x10^5$ steps) and subsequently the NPT ensemble (100 ps, $1x10^5$ steps), both employing a coupling constant of 0.1 ps. Finally, a production MD run was executed for 5 million steps (step size 2 fs), yielding a total simulation duration of 100 ns. Following simulation, the Gromacs toolkit was employed for trajectory analysis. The binding free energy was calculated using the Molecular Mechanics/Generalized Born Surface Area (MM/GBSA) method (18), complemented by analyses of protein structural dynamics including the radius of gyration, root-mean-square deviation (RMSD) and root-mean-square fluctuation (RMSF).

In vitro validation experiments

Cell Counting Kit (CCK)-8 assay. Logarithmically growing HepG2 cells were inoculated into 96-well plates ($1x10^4$ cells/well). This was followed by a 24 h incubation under conditions (37˚C; 5% CO_2) to allow cell adhesion. Cells were then treated for 24 h with test agents: AS (0, 10, 20, 30 and 40 mg/ml), BS (0, 20, 40, 80 and 160 μg/ml, solvent: ethanol), or ST (0, 40, 80, 120 and 160 μg/ml, solvent, acetone). A 100 μl aliquot of CCK-8 working solution (prepared from 90 μl DMEM and 10 μl CCK-8 reagent; cat. no. C0037; Beyotime Biotechnology) was dispensed into each well. Wells containing medium only were designated as blank controls. After a further 30 min incubation, cell viability was assessed by measuring the absorbance at 450 nm for each well with a microplate reader. The half-maximal inhibitory concentration (IC_{50}) was calculated using GraphPad Prism 8.0 (Dotmatics).

Colony formation assay. HepG2 cells were seeded into 6-well plates ($3x10^3$ cells/well). After 1 day of incubation for adhesion, cells were treated with the two agents for 10-14 days at 37˚C: AS (0, 5, 10 and 20 mg/ml) and BS (0, 10, 20 and 40 μg/ml). When cell colonies grew to 1-2 mm in diameter, the culture was terminated. The colonies were processed by fixation in 4% paraformaldehyde (PFA) for 30 min at room temperature (RT) in the dark. After fixation, colonies were stained with 0.1% crystal violet solution for 20 min (RT, protected from light). The number of colonies (defined as clusters of >50 cells) after staining was analyzed using ImageJ software (version 1.51w; https://imagej.net/ij/).

Wound healing assay. HepG2 cells were seeded in 6-well plates ($2.7x10^6$ cells/well). They were cultured for 24 h to ~90% confluence. Upon reaching confluence, a sterile 10 μl pipette tip was drawn across the monolayer to generate a uniform scratch. Cells were then treated with low-serum medium (containing 2% FBS; cat. no. 11965092; Gibco; Thermo Fisher Scientific, Inc.) supplemented with different concentrations of either AS (0, 5, 10 and 20 mg/ml) or BS (0, 10, 20 and 40 μg/ml). Wound closure was tracked and recorded at the indicated time intervals (0, 24, 48 and 72 h post-treatment) using an inverted phase-contrast microscope, followed by semi-quantitative analysis (gray value measurement) of the acquired images with ImageJ software.

TUNEL staining. For subsequent assays, aseptic coverslips were positioned in 24-well plates prior to the seeding of viable HepG2 cells at a final density of $2x10^4$ cells/well. The groups were set as follows: i) Blank control; ii) pathway inhibitor PFT-α (20 μM) group; iii) BS (40 μg/ml) group; and iv) PFT-α (20 μM) + BS (40 μg/ml) combination treatment group. After a 2 day culture, cells were sequentially subjected to the following procedures: Fixation with 4% PFA (20 min; 25˚C), permeabilization with 0.1% Triton X-100 (10 min; 25˚C), TUNEL staining was performed for 60 min at 37˚C (cat. no. C1086; Beyotime Biotechnology), DAPI nuclear counterstaining (1 μg/ml; 10 min at 25˚C, protected from light) and mounting with an anti-fade mounting medium, followed by fluorescence microscopy imaging (five random fields of view per sample).

Transwell migration assay. HepG2 cells were loaded into the upper inserts at the designated density ($3x10^5$ cells/insert) in serum-free DMEM, while the lower chambers were loaded with complete medium (DMEM containing 10% FBS). Cells were treated for 3 days at 37˚C with medium containing different concentrations of AS (0, 5, 10 and 20 mg/ml) or BS (0, 10, 20 and 40 μg/ml). After treatment, the post-migration cells on the lower membrane surface were processed for fixation and staining (4% PFA and crystal violet, respectively, at RT for 30 min in the dark)., rinsed with PBS, and then observed and counted under a microscope (upright light microscope; Olympus BX63; Olympus Corporation).

Immunofluorescence staining. Prior to cell seeding, aseptic coverslips were positioned in 24-well plates, followed by plating HepG2 cells at a final density of $2x10^4$ cells/well. After

cell adherence and reaching suitable density, cells were fixed with 4% PFA for 20 min at 25˚C. Samples were first processed for permeabilization (0.3% Triton X-100) and blocked with 5% BSA for 60 min at 25˚C to minimize non-specific binding. They were then incubated with diluted primary antibodies (Bcl-2, 1:200, cat. no. 26593-1-AP; Bax, 1:200, cat. no. 50599-2-Ig; p53, 1:800, cat. no. 60283-2-Ig; MMP2, 1:500, cat. no. 10373-2-AP; MMP9, 1:400, cat. no. 10375-2-AP; all from Proteintech Group, Inc.) at 4˚C overnight. Subsequently, secondary antibodies (Alexa Fluor 488-conjugated goat anti-rabbit IgG or Alexa Fluor 594-conjugated goat anti-mouse IgG, both 1:500; cat. nos. A11008 and A11032; Thermo Fisher Scientific, Inc.) were applied (incubated for 1 h at RT, protected from light). After PBS washing, nuclei were counterstained with DAPI solution (incubated for 5 min at RT, shielded from light). Excess dye was removed by washing with PBS, and the samples were mounted for fluorescence microscopy.

Western blot analysis. HepG2 cells were lysed on ice using RIPA lysis buffer (cat. no. P0013B; Beyotime Biotechnology) supplemented with 1% phenylmethylsulfonyl fluoride for 30 min. Centrifugation was performed at 14,000 x g for 10 min at 4˚C. The supernatant, free of insoluble material, was then carefully collected. BCA method was employed to determine the protein concentration. Protein samples (equal amounts, 30 μg per lane) were processed through sequential electrophoretic separation on SDS-polyacrylamide gels (10% separating gel and 5% stacking gel) and electroblotting onto PVDF membranes. The membranes were blocked with rapid blocking buffer for 20 min at RT and washed three times with TBST (0.1% Tween-20). The membranes were then probed with primary antibodies (Bcl-2, 1:1,000 cat. no. 26593-1-AP; Bax, 1:20,000, cat. no. 50599-2-Ig; p53, 1:5,000, cat. no. 60283-2-Ig; MMP2, 1:500, cat. no. 10373-2-AP; MMP9, 1:500, cat. no. 10375-2-AP; cleaved Caspase-3, 1:1,000, cat. no. 25128-1-AP; Caspase-3,1:1,000, cat. no. 19677-1-AP; GAPDH, 1:50,000, cat. no. 60004-1-Ig; β-Tubulin, 1:20,000 cat. no. 66240-1-Ig; all from Proteintech Group, Inc.) overnight at 4˚C. After TBST washes, HRP-linked secondary antibodies (HRP-conjugated goat anti-rabbit IgG or HRP-conjugated goat anti-mouse IgG, both 1:5,000; cat. nos. SA00001-2 and SA00001-1; Proteintech Group, Inc.) were subjected to a 1 h incubation at RT. Following thorough washing, protein bands were visualized using ECL chemiluminescent substrate (Thermo Fisher Scientific, Inc.). The acquired Western blot analysis images were subjected to densitometric semi-quantification to determine band intensities, utilizing ImageJ software (version 1.51w) for the analysis.

Statistical analysis. Data were presented as mean ± standard deviation, and all experiments were performed with three independent biological repeats (n=3). All analyses were performed in GraphPad Prism 8.0. For multiple-group datasets, a one-way ANOVA was performed. The following three a-priori planned pairwise comparisons were tested following one-way ANOVA with Bonferroni post hoc correction: Blank control vs. inhibitor-only group, blank control vs. drug-only group and drug-only group vs. drug-inhibitor co-treatment group. The Bonferroni correction factor was set to m=3 and a corrected $P<0.05$ was considered to indicate a statistically significant difference. For other datasets where each experimental group was only compared against the blank control group, the one-way ANOVA was followed by Dunnett's post hoc test. For wound-healing assays, a one-way ANOVA followed by Dunnett's post hoc test was performed at each individual time point. $P<0.05$ was considered to indicate a statistically significant difference.

Results

Shared AS-liver cancer target network and PPI analysis. The database search identified 299 and 1,601 targets associated with AS and liver cancer, respectively. A total of 67 shared targets were identified by Venn diagram analysis (Fig. 1A). To examine the interactions between the overlapping targets, a PPI network was built (Fig. 1B). After network optimization by removing unconnected nodes, the network was visualized in Cytoscape based on the exported TSV file (Fig. 1C).

Network parameters for network nodes were calculated for: i) CC; ii) degree; iii) BC; iv) NC; v) EC; and vi) LAC. Initial screening was performed with the median value of each parameter as the threshold. The specific criteria were: BC ≥30.4474, CC ≥0.4672, degree ≥16, EC ≥0.0622, LAC ≥8 and NC ≥8.8889. This step identified 24 candidate core targets.

A subnetwork built from these 24 targets was then screened in a second round. Thresholds, also based on median values, were set as follows: BC ≥5.6617, CC ≥0.7799, degree ≥49.5, EC ≥0.2169, LAC ≥36.3529 and NC ≥39.8486. Finally, 9 central targets were identified. This hierarchical screening workflow is illustrated in Fig. 1D and the corresponding topological parameters of each core target are listed in Table I.

AS inhibits the proliferation and migration of HepG2 cells. To assess the effect of AS on HepG2 cells, a CCK-8 assay was carried out to measure the viability of HepG2 cells after 24 h treatment with AS (10, 20, 30 and 40 mg/ml). AS reduced cell viability in a dose-dependent manner, with a calculated IC_{50} value of 20.68 mg/ml (Fig. 2A). Based on this result, subsequent experiments used AS at the following concentrations of 0, 5, 10 and 20 mg/ml.

The clonogenic capacity of HepG2 cells was assessed with a colony formation assay. Colony formation significantly decreased in a dose-dependent manner in AS-treated groups compared with the control (Fig. 2B).

To test whether AS affected migration of HepG2 cells, wound-healing and Transwell assays were conducted. Wound healing assay results revealed that the scratch closure of HepG2 cells was suppressed by AS over time and with increasing concentration (Fig. 2C). After 48 h of treatment at 10 and 20 mg/ml AS, the wound-closure rate was significantly decreased compared with the control group. After 72 h of treatment, the wound-closure rate was significantly decreased in all AS treatment groups, with a marked decrease in wound healing rate in the AS groups compared with the control. Transwell assay results also confirmed that AS significantly reduced the number of cells that migrated in a dose-dependent manner, indicating its effective suppression of the Transwell migration of HepG2 cells (Fig. 2D).

AS inhibits the expression of MMP-2 and MMP-9. MMP-2 and MMP-9, zinc-dependent endopeptidases, are associated with

Table I. Core targets of AS against liver cancer and their topological parameters identified through a two-stage screening strategy.

Name	BC	CC	Degree	EC	LAC	NC
INS	17.2707	0.9200	63	0.2567	40.8571	55.5450
PPARG	16.5138	0.9200	63	0.2590	41.7143	56.0637
NFKB1	13.1058	0.8846	60	0.2503	40.8000	51.8460
ESR1	12.7201	0.8846	60	0.2509	41.1000	52.0004
ALB	15.0111	0.8846	60	0.2467	39.6000	51.1495
BCL2	8.3351	0.8214	54	0.2309	39.3333	45.6825
TNF	8.0683	0.8214	54	0.2322	39.3333	45.2208
PTGS2	10.5676	0.8214	54	0.2272	37.3333	43.8262
SREBF1	7.3953	0.7931	51	0.2209	36.7059	40.4736

ALB, albumin; AS, *Angelica sinensis*; BC, Betweenness centrality; CC, Closeness centrality; EC, Eigenvector Centrality; ESR1, estrogen receptor 1; INS, insulin; LAC, Local average connectivity; NC, Network centrality; NFKB1, nuclear factor κB subunit 1; PPARG, peroxisome proliferator-activated receptor γ; PTGS2, prostaglandin-endoperoxide synthase 2; SREBF1, sterol regulatory element-binding transcription factor 1.

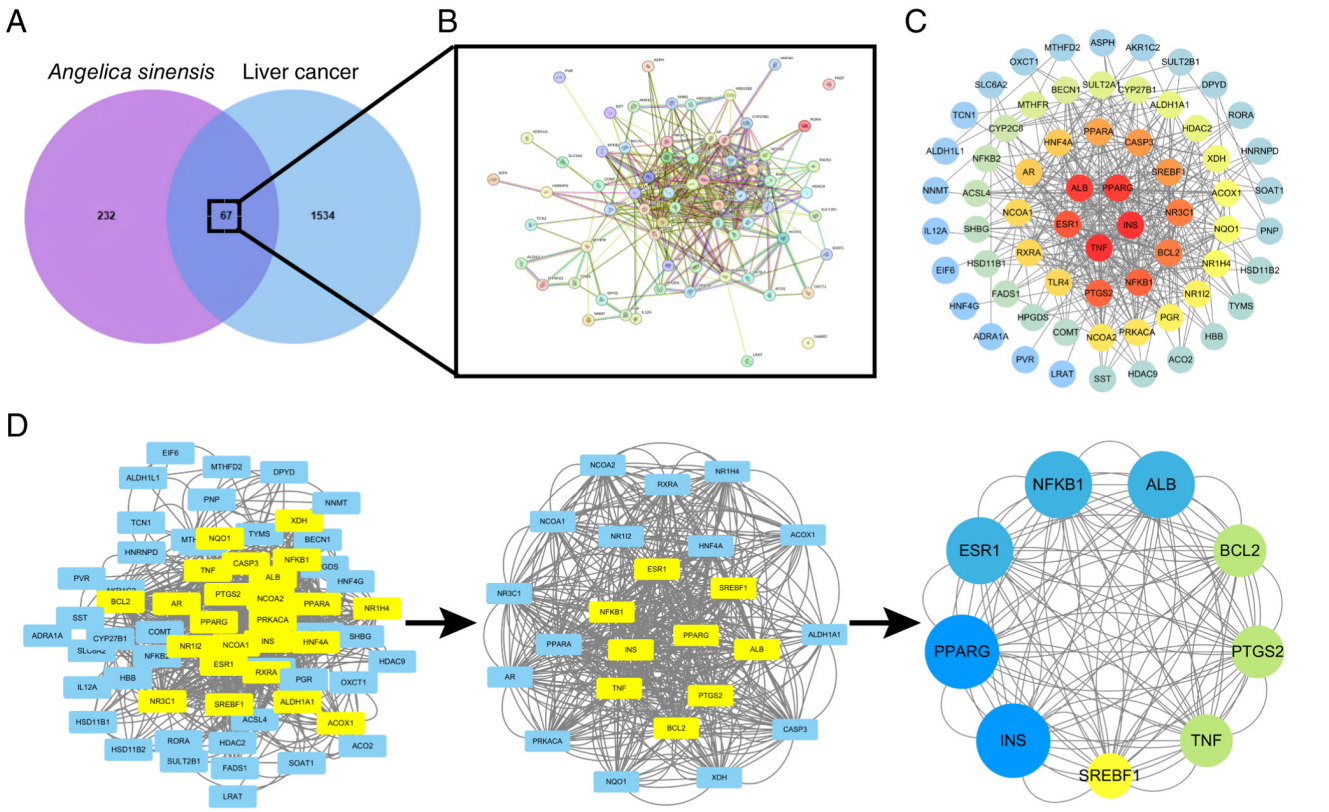
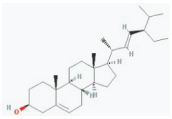
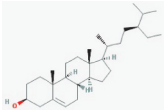


Figure 1. Network pharmacology of AS in the context of liver cancer. (A) Venn analysis illustrating the overlapping targets between AS and liver cancer. (B) Topological graph of the PPI network. (C) Visualization of the PPI network generated using Cytoscape software. (D) Workflow for screening core AS-liver cancer targets based on network centrality analysis. AS, *Angelica sinensis*; PPI, protein-protein interaction.

tumor metastasis, invasion and poor prognosis in liver cancer. Because they are often overexpressed, they are regarded as important molecular markers for assessing liver cancer malignancy (19,20). To determine whether AS affected liver cancer progression by regulating MMPs, immunofluorescence staining was used to assess changes in MMP-2 and MMP-9 expression after 24 h treatment of HepG2 cells with varying AS concentrations. The results shown in Fig. 3 indicated that as AS concentrations increased, the fluorescence intensities of MMP-2 and MMP-9 significantly decreased in a dose-dependent manner, suggesting that AS downregulated the expression of both proteins. Together, these findings suggest that AS may inhibit the invasive and migratory capacities of HepG2 cells by suppressing the expression of MMP-2 and MMP-9, possibly by limiting extracellular matrix degradation, thereby contributing to its antimetastatic effect.

Table II. Screening results of active components from AS (OB ≥30% and DL ≥0.18).

Structure	Mol ID	Name	MW	ALogP	OB (%)	DL
	MOL000449	Stigmasterol	412.77	7.64	43.83	0.76
	MOL000358	β-sitosterol	414.79	8.08	36.91	0.75

AS, *Angelica sinensis*; DL, drug-likeness; MW, molecular weight; OB, oral bioavailability.

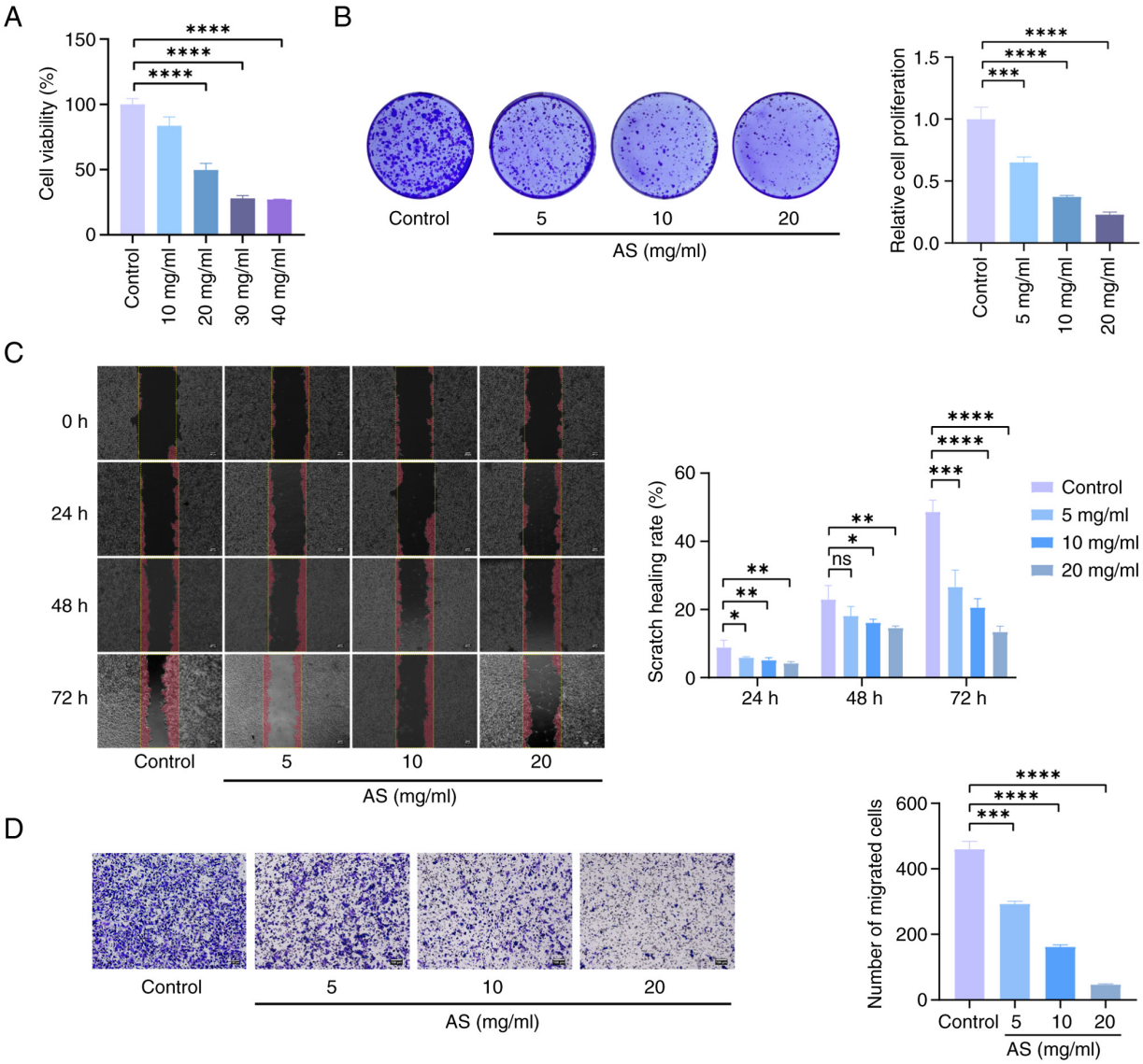


Figure 2. Impact of AS on the viability and migratory capacity of HepG2 cells. (A) Cell viability after AS treatment (CCK-8 assay). (B) Proliferation inhibition assessed by colony formation. (C) Representative results of the cell scratch assay, showing the inhibitory effect of AS on the lateral migration of HepG2 cells, (magnification, x4; scale bar, 200 μm). (D) Transwell assay was used to evaluate AS-mediated inhibition of HepG2 cell vertical migration, (magnification, x10; scale bar, 100 μm). *P<0.05, **P<0.01 and ***P<0.001, ****P<0.0001. AS, *Angelica sinensis*; CCK, Cell Counting Kit; ns, not significant.

Molecular docking of AS bioactives to core targets. The chemical constituents of AS were obtained from the TCMSP database collection. The active components were screened using drug-likeness (DL ≥0.18) and oral bioavailability (OB ≥30%) (Table II). The representative components, BS and ST, were selected for molecular docking with five core targets: INS,

Table III. Molecular docking of representative components and core targets.

Target	Binding energy (BS) (kcal/mol)	Binding energy (ST) (kcal/mol)	ΔΔG (ST-BS)	Key hydrogen bonds of BS	Key hydrogen bonds of ST
PPARG	-10.1	-7.6	+2.5	GLU-259 (2.2 Å)	-
ALB	-8.5	-7.3	+1.2	-	-
NFKB1	-7.0	-6.5	+0.5	GLU-62 (2.3 Å)	-
ESR1	-6.9	-6.7	+0.2	LYS-492 (2.5 Å)	SER-309 (2.3 Å)
INS	-7.6	-8.0	-0.4	-	-

The conclusions in this table are based on a comprehensive analysis of the predicted binding free energy difference (ΔΔG) and interaction patterns. According to the widely adopted empirical criterion in the field, ΔΔG >1.0 kcal/mol is considered indicative of a clear preference, while ΔΔG >2.0 kcal/mol accompanied by key interactions (for example hydrogen bonds) is regarded as significantly stronger binding. ALB, albumin; BS, β-sitosterol; ESR1, estrogen receptor 1; INS, insulin; NFKB1, nuclear factor κB subunit 1; PPARG, peroxisome proliferator-activated receptor γ; ST, Stigmasterol.

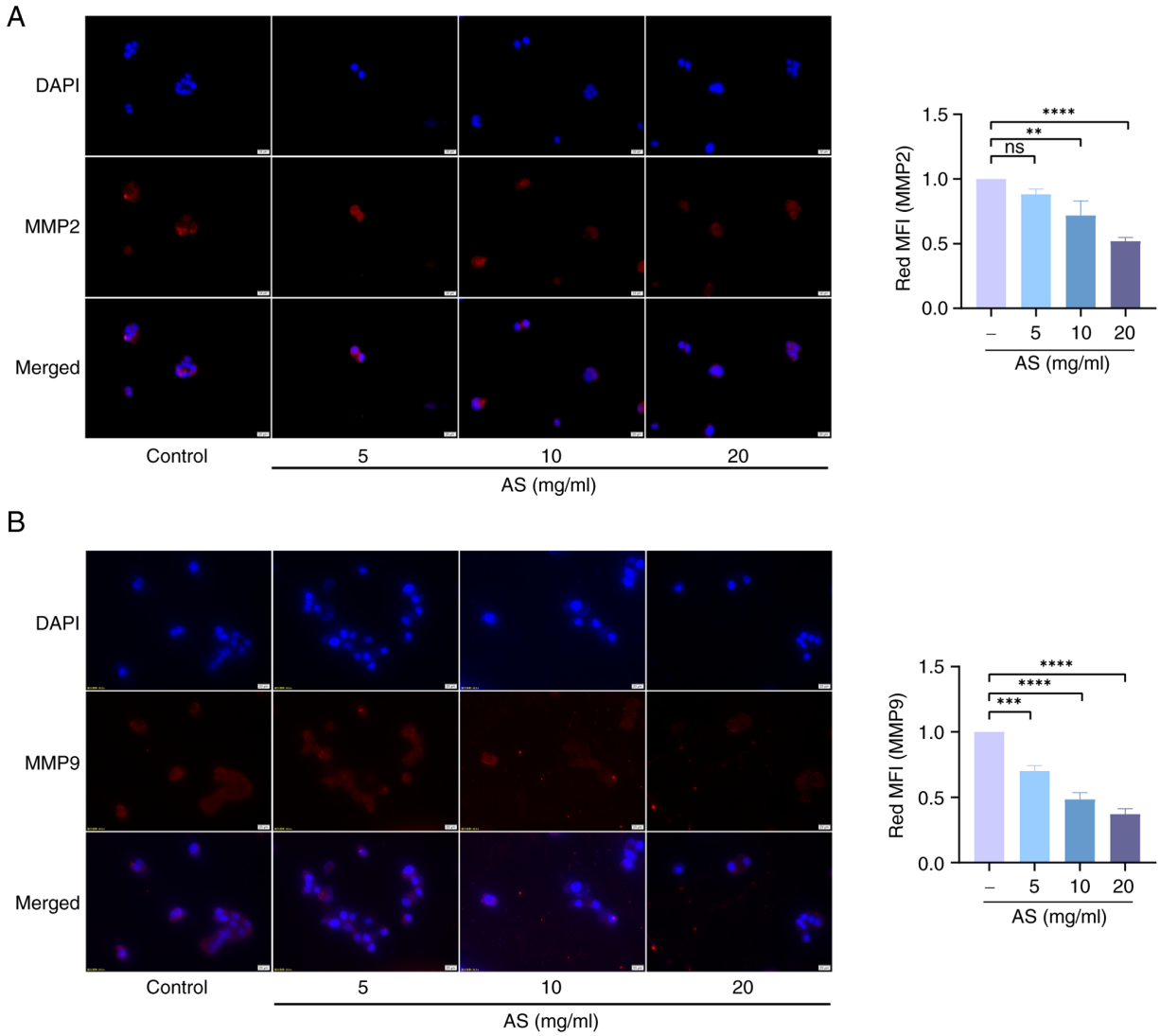


Figure 3. Effect of AS on the expression of MMP-2 and MMP-9 proteins in HepG2 cells. (A) Immunofluorescence staining of MMP-2. (B) Immunofluorescence staining of MMP-9, (magnification, x40; scale bar, 20 μm). **P<0.01, ***P<0.001 and ****P<0.0001. AS, *Angelica sinensis*; MFI, mean fluorescence intensity; ns, not significant.

PPARG, NFKB1, ESR1 and ALB. Based on docking energies (Table III), a heatmap was built (Fig. 4A). All active components bound to the central targets with energies below -5 kcal/mol, indicating a favorable binding affinity (21). Furthermore, the

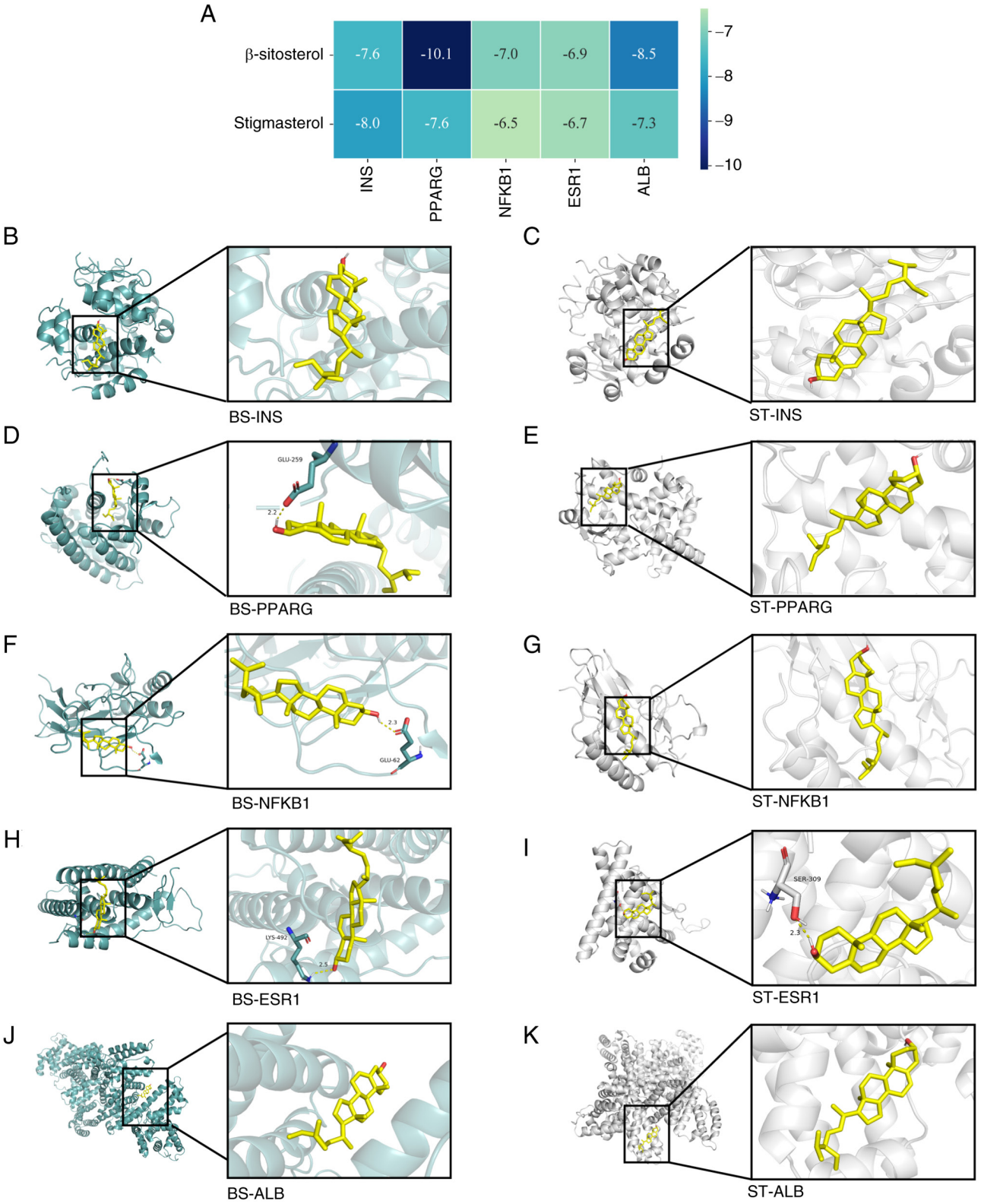


Figure 4. Molecular docking results. (A) Affinity heatmap visualizing docking scores between AS constituents and core targets (kcal/mol). (B) Binding modes of BS and INS. (C) Binding modes of ST and INS. (D) Binding modes of BS and PPARG. (E) Binding modes of ST and PPARG. (F) Binding modes of BS and NFKB1. (G) Binding modes of ST and NFKB1. (H) Binding modes of BS and ESR1. (I) Binding modes of ST and ESR1. (J) Binding modes of BS and ALB. (K) Binding modes of ST and ALB. The Protein Data Bank IDs of the target proteins used for molecular docking are as follows: INS (6TC2), PPARG (9F7X), NFKB1 (8TQD), ESR1 (7UJ8), ALB (8RGL). ALB, albumin; AS, *Angelica sinensis*; BS, β-sitosterol; ESR1, estrogen receptor 1; INS, insulin; NFKB1, nuclear factor κB subunit 1; PPARG, peroxisome proliferator-activated receptor γ; ST, Stigmasterol

3D interaction patterns between BS/ST and each target were visualized using PyMOL software (Fig. 4B-K).

Docking results showed that BS formed stable hydrogen bonds with central targets such as PPARG, NFKB1 and ESR1.

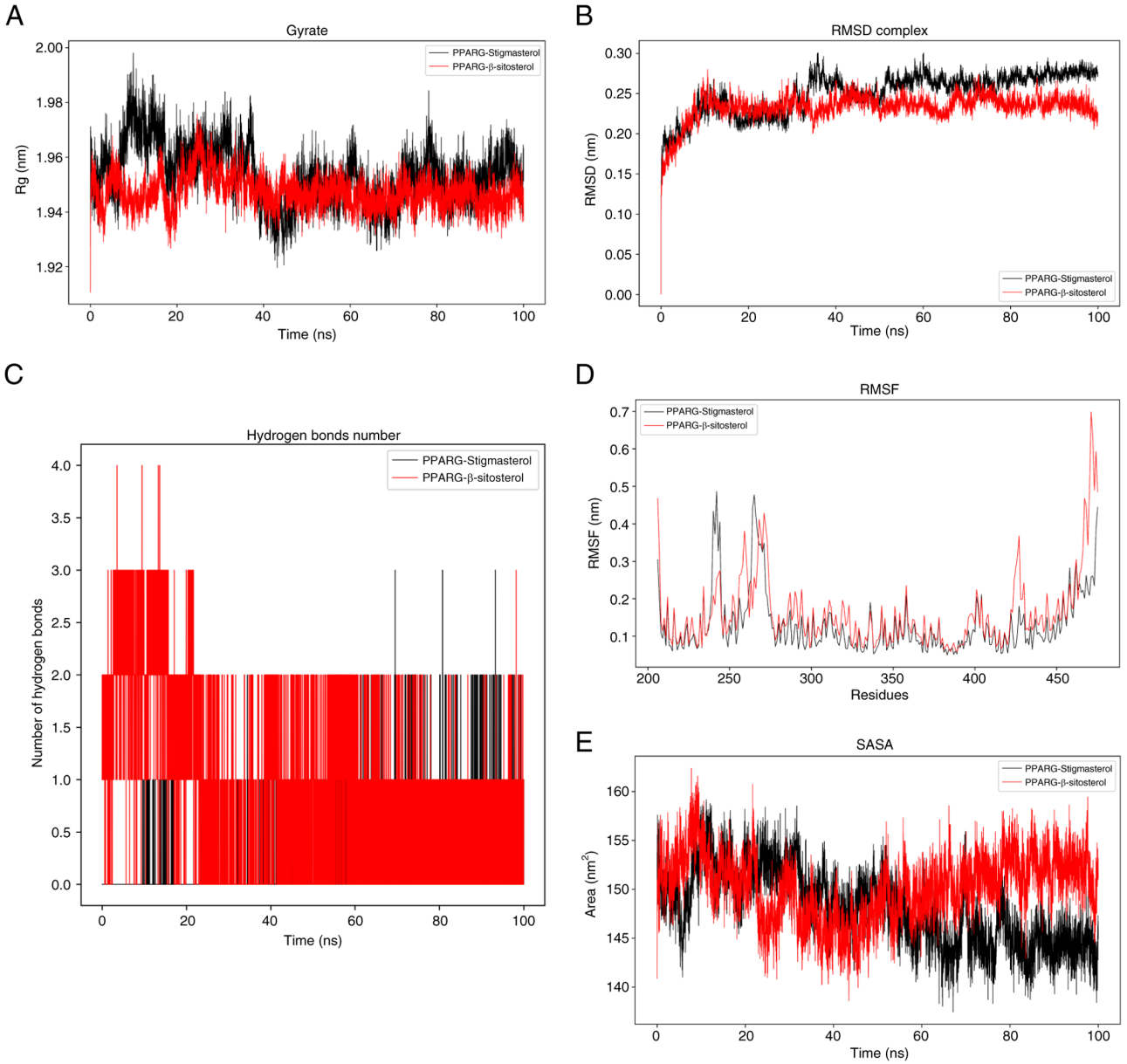


Figure 5. Analysis of MD simulation results. (A) Rg of the two complexes. (B) RMSD of the two complexes. (C) Number of hydrogen bonds in the two complexes. (D) RMSF of the two complexes. (E) SASA of the two complexes. PPARG, peroxisome proliferator-activated receptor γ; Rg, radius of gyration; RMSD, root mean square deviation; RMSF, root mean square fluctuation; SASA, solvent accessible surface area.

For instance, it formed a hydrogen bond of 2.2 Å with the GLU-259 residue of PPARG, and its lower binding free energy (-10.1 kcal/mol) suggested more stable binding. By contrast, ST formed a hydrogen bond with only ESR1, exhibited a less negative binding free energy (-6.7 kcal/mol), and showed no clear hydrogen bonding with the other targets, suggesting weaker stability. Further analysis indicated that binding free energy of BS for PPARG was ~2.5 kcal/mol lower than that of ST, equivalent to ~100-fold increase in binding affinity, implying that BS may bind more strongly. To test these static docking results and assess the interactions in a dynamic system, MD simulations were then performed.

Analysis of MD simulation results. In the MD simulations, 100 ns trajectories were generated on the protein-ligand complex systems formed between PPARG and ST or BS to evaluate their structural stability and binding affinity. The results indicated that the two systems remained overall stable; however, the performance of the PPARG-BS system was improved in several metrics, suggesting that BS binds to PPARG more tightly and stably.

First, the structural compactness was assessed by monitoring its radius of gyration (Rg). The average Rg values were 1.95±0.01 nm for the two systems, with small standard deviations, showing that the protein maintained a compact conformation throughout the simulation and exhibited no obvious unfolding or large-scale conformational changes, consistent with structural stability (Fig. 5A).

Second, RMSD was used to monitor structural changes. The complex RMSD (RMSD-complex) was 0.25±0.03 nm for the PPARG-ST system and 0.23±0.02 nm for the PPARG-BS system, both remaining below 0.3 nm, indicating structural

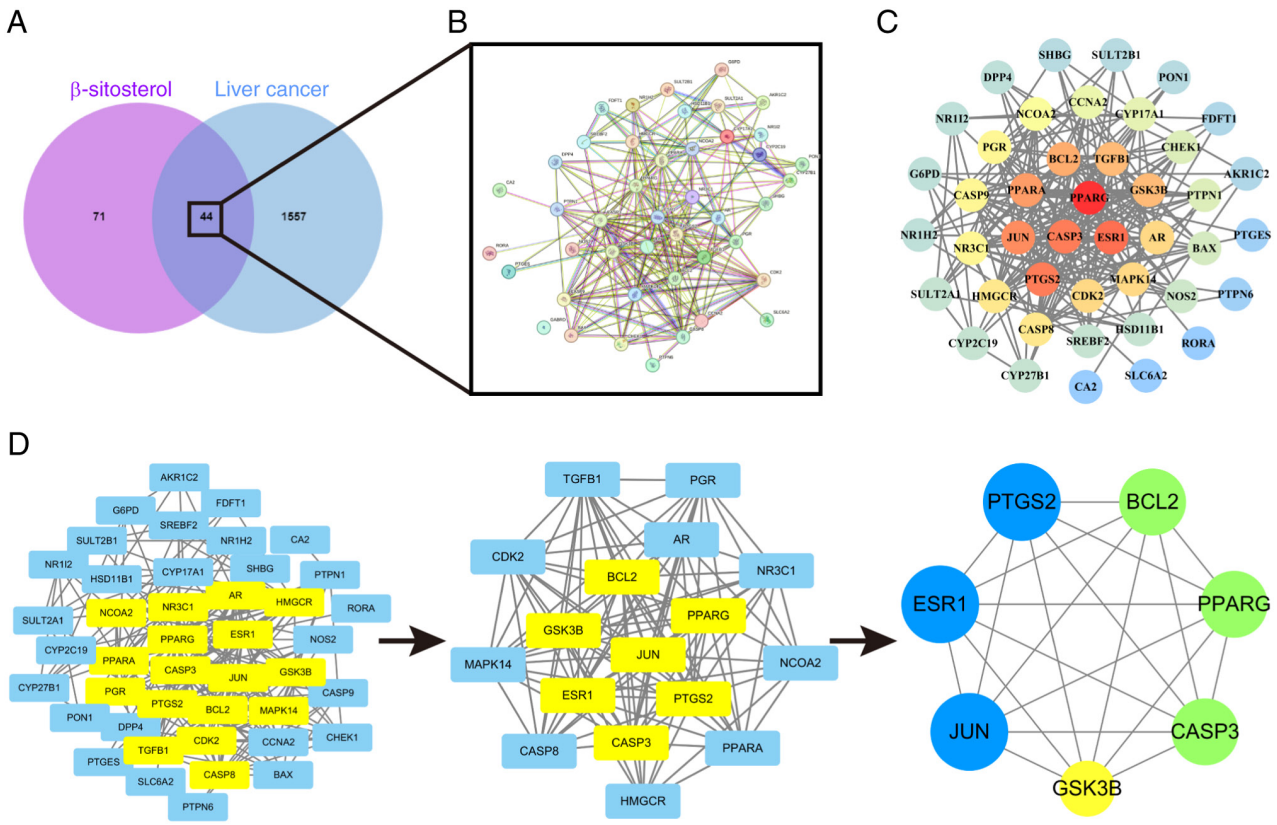


Figure 6. Network pharmacology-based analysis for the anti-liver cancer activity of BS. (A) Venn diagram depicting shared targets for BS and liver cancer. (B) Topological graph of the PPI network. (C) Visualization of the PPI network generated using Cytoscape software. (D) Workflow for screening core BS-liver cancer targets based on network centrality analysis. BS, β-sitosterol; PPI, protein-protein interaction.

stability in the two systems. The BS system displayed a lower and smaller RMSD fluctuation. Ligand RMSD (RMSD-lig) was 0.09±0.01 nm for PPARG-ST and 0.07±0.01 nm for PPARG-BS, suggesting greater positional stability of BS within the ligand-binding pocket. Protein RMSD (RMSD-pro) was 0.18±0.02 nm in the two systems, also supporting the stability of the protein backbone (Fig. 5B).

Hydrogen-bond analysis examined the interactions stabilizing the protein-ligand complexes. The average number of protein-ligand hydrogen bonds in the PPARG-ST system was 0.22±0.44, indicating infrequent, unstable hydrogen bonding, with an average value close to zero. By contrast, the PPARG-BS system showed an average of 0.88±0.95 hydrogen bonds, roughly corresponding to one persistent bond, indicating more frequent and stable hydrogen-bond interactions that may enhance binding affinity (Fig. 5C).

RMSF was used to evaluate the flexibility of individual protein residues. The average RMSF was 0.13±0.08 nm for PPARG-ST and 0.16±0.10 nm for PPARG-BS. Both values were relatively low (<0.2 nm), indicating limited residue flexibility of the protein residues and no significant local unfolding or unstable local regions. Although the BS system showed a slightly higher RMSF, it remained within an acceptable range, and the standard deviation suggested that fluctuations were mostly concentrated in non-critical regions (Fig. 5D).

Solvent-accessible surface area (SASA) was used to assess changes in the protein solvent-exposed surface. The average SASA was 148.06±3.82 nm^2 for the PPARG-ST system and 150.19±3.33 nm^2 for the PPARG-BS system. The values were similar, with only small fluctuations, indicating stable solvent exposure of the protein surface without major changes due to ligand binding. The slightly higher SASA in the BS system might be related to minor local adjustments in the ligand-binding pocket, while overall solvent exposure remained well-maintained (Fig. 5E).

To quantify the ligand-protein affinity, binding free energy (ΔG) was estimated using the MM/GBSA approach. The results (Table IV) showed that the total binding free energy was -40.65±0.76 kcal/mol for the PPARG-ST system and -53.57±1.39 kcal/mol for the PPARG-BS system. The lower binding free energy of the BS system was

Table IV. Calculated binding free energies.

Contribution components	PPARG-ST	PPARG-BS
ΔVDWAALS	-49.18±0.08	-57.05±1.15
ΔEelec	-1.83±0.73	-8.74±0.75
ΔEGB	16.45±0.21	19.50±0.26
ΔEsurf	-6.09±0.01	-7.27±0.03
ΔGgas	-51.01±0.73	-65.79±1.37
ΔGsolvation	10.36±0.21	12.23±0.26
ΔTotal	-40.65±0.76	-53.57±1.39

BS, β-sitosterol; PPARG, peroxisome proliferator-activated receptor γ; ST, Stigmasterol.

Table V. Core targets of BS against liver cancer and their topological parameters identified through a two-stage screening strategy.

Name	Degree	CC	BC	EC	NC	LAC
JUN	16	1.0000	6.1074	0.2838	16.0000	11.8750
PTGS2	16	1.0000	6.1074	0.2838	16.0000	11.8750
ESR1	16	1.0000	6.1074	0.2838	16.0000	11.8750
CASP3	15	0.9412	4.0605	0.2727	14.4475	11.6000
PPARG	15	0.9412	5.2509	0.2684	14.2018	11.2000
BCL2	15	0.9412	4.0605	0.2727	14.4475	11.6000

CC, closeness centrality; BC, betweenness centrality; EC, Eigenvector centrality; NC, network centrality; LAC, local average connectivity.

primarily attributed to stronger van der Waals interactions (ΔVDWAALS: -57.05±1.15 kcal/mol vs. -49.18±0.08 kcal/mol) and electrostatic interactions (ΔEelec: -8.74±0.75 kcal/mol vs. -1.83±0.73 kcal/mol), supporting stronger binding than ST.

Taken together, the 100 ns MD simulations showed that both PPARG-ST and PPARG-BS complex systems remained structurally stable, as reflected by RMSD, Rg and RMSF remaining at low levels and no obvious perturbation of the protein structure. However, the PPARG-BS system showed an advantage over the PPARG-ST system for hydrogen-bond number, ligand RMSD and binding free energy, indicating stronger binding affinity and a more stable interaction. These findings suggest that BS appears to be a stronger ligand candidate for PPARG with greater potential bioactivity. Supported by subsequent CCK-8 assays, confirming the stronger antiproliferative activity of BS, the present study selected BS for further study, including mechanistic investigation.

BS-liver cancer common target network construction and core pathway enrichment. Overall, 115 BS-related targets and 1,601 liver cancer-related targets were retrieved from the databases. Cross-comparison identified 44 shared targets (Fig. 6A), suggesting that these targets may contribute to the anti-liver cancer efficacy of BS. A PPI network was generated from the STRING database, comprising 44 nodes and 490 interaction edges (Fig. 6B), and also visualized after optimization in Cytoscape (Fig. 6C).

The following network parameters were calculated for each node: i) EC; ii) degree; iii) BC; iv) LAC; v) CC; and vi) NC. Using the median value of each parameter as the initial cutoff (BC ≥12.91, CC ≥0.512, degree ≥10, EC ≥0.122, LAC ≥6 and NC ≥7.714), 17 candidate core targets were obtained. A subnetwork was built with these targets and screened again with stricter cutoffs based on median values (BC ≥2.549, CC ≥0.842, degree ≥13, EC ≥0.240, LAC ≥10.333 and NC ≥11.612), yielding 7 central targets. The screening workflow is depicted in Fig. 6D, and the detailed network indices of each target are listed in Table V.

To define the biological roles of the central targets, enrichment analysis was performed for both GO functions and KEGG pathways, using a cutoff of P<0.05. GO analysis identified 2,772 entries, including 2,398 biological processes (BP), 249 molecular functions (MF) and 125 cellular components (CC). The top 10 results revealed that BP terms mainly involved 'intracellular receptor signaling pathways' and the 'regulation of steroid/lipid metabolism' (Fig. 7A), CC terms were concentrated in 'membrane raft', 'membrane microdomain' and 'organelle outer membrane' (Fig. 7B), and MF terms were mainly associated with 'nuclear receptor activity', 'transcription cofactor binding' and 'steroid hormone receptor activity' (Fig. 7C). A bar graph of the top 10 GO entries ranked by enrichment score is presented in Fig. 8A. KEGG analysis identified 184 pathways, with the top 30 enriched in the 'p53 pathway' (Fig. 9), 'apoptosis-multiple species', 'hepatitis B', 'non-alcoholic fatty liver disease' and other pathways (Fig. 8B). Finally, an integrated 'BS-liver cancer-target-pathway' network was built (Fig. 8C). This network contained multiple targets and related pathways, suggesting that the anti-liver cancer efficacy of BS may rely on its multitarget and multipathway regulatory pattern.

Effects of the AS active components BS and ST on the viability and proliferation of HepG2 Cells. Fig. 10A shows the molecular structure of BS. CCK-8 assay results showed that BS inhibited the viability of HepG2 cells dose-dependently, with a calculated IC_{50} of 41.19 μg/ml (Fig. 10B). The molecular structure of ST is shown in Fig. 10C. The CCK-8 assay identified an IC_{50} of 50.93 μg/ml for ST (Fig. 10D). To investigate the effects of BS on cellular functions at sub-cytotoxic concentrations, subsequent experiments focused on its effects on malignant phenotypes within the subcytotoxic concentration range. Accordingly, a subcytotoxic concentration range of 10-40 μg/ml (below the IC_{50}) was used for the experimental groups. As expected, a colony formation assay confirmed that, within this concentration range, BS significantly reduced the colony-forming ability of HepG2 cells (Fig. 10E).

BS inhibits the migration of HepG2 cells. Metastasis is a major determinant of poor outcomes in cancer. Therefore, the present study investigated whether BS affects migration using wound-healing and Transwell assays. Image analysis showed that the wound-closure rate in the BS-treated groups was slower than the control group in the wound healing assay (Fig. 11A). The wound closure decreased with increasing drug concentrations, suggesting that BS reduced the lateral migratory capacity of HepG2 cells dose-dependently. The Transwell assay confirmed a consistent trend in cell migratory ability, showing that BS significantly reduced Transwell migration of HepG2 cells in a dose-dependent manner (Fig. 11B). Together,

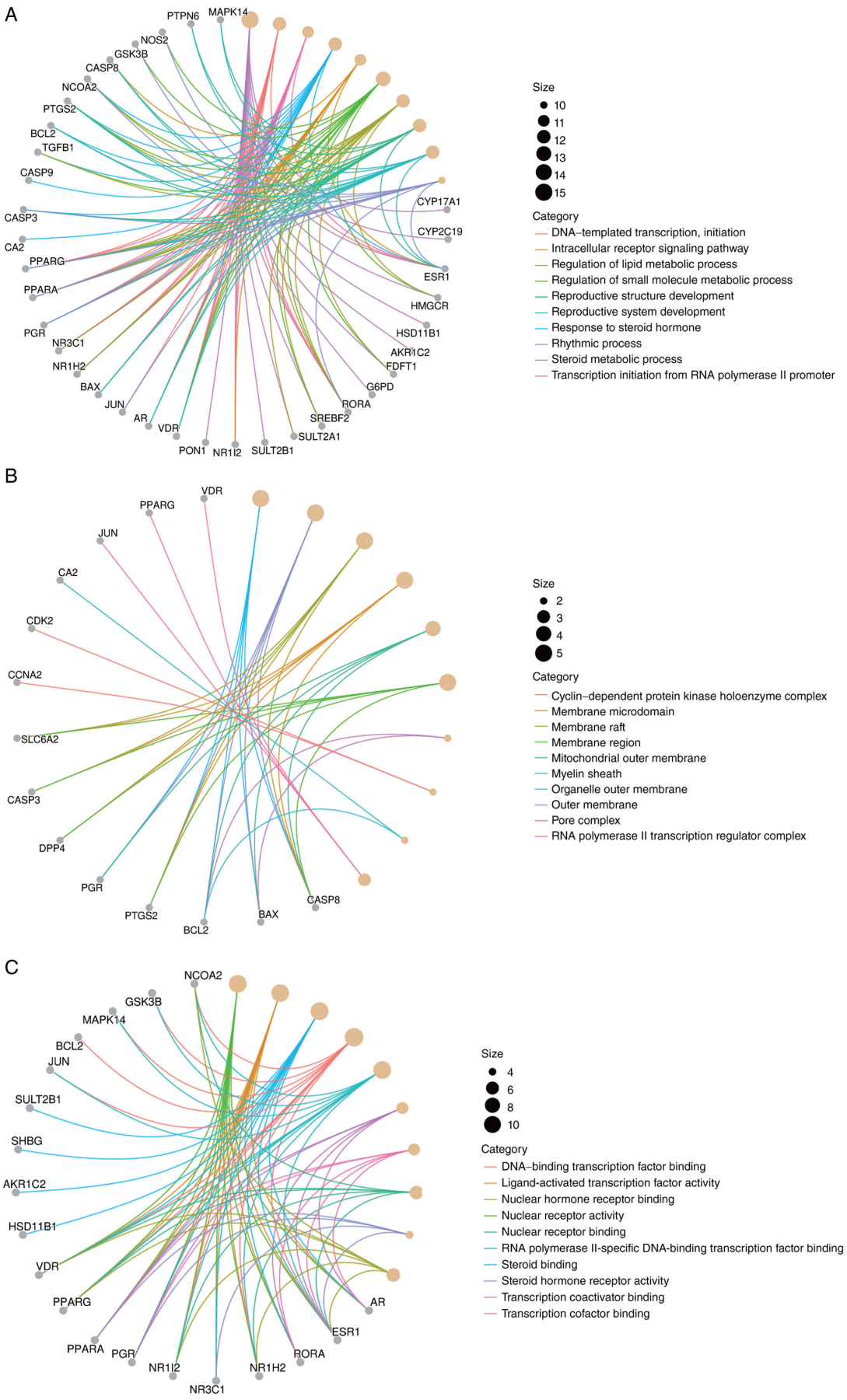


Figure 7. Gene Ontology functional enrichment analysis of shared targets between BS and liver cancer. Gray represents genes and ochre represents biological processes. The connecting lines between genes and biological processes represent the genes involved in each biological process. The size of the circles represents the number of genes contained in each biological process. (A) Biological processes of the common targets. (B) Cellular components of the common targets. (C) Molecular functions of the common targets. BS, β-sitosterol.

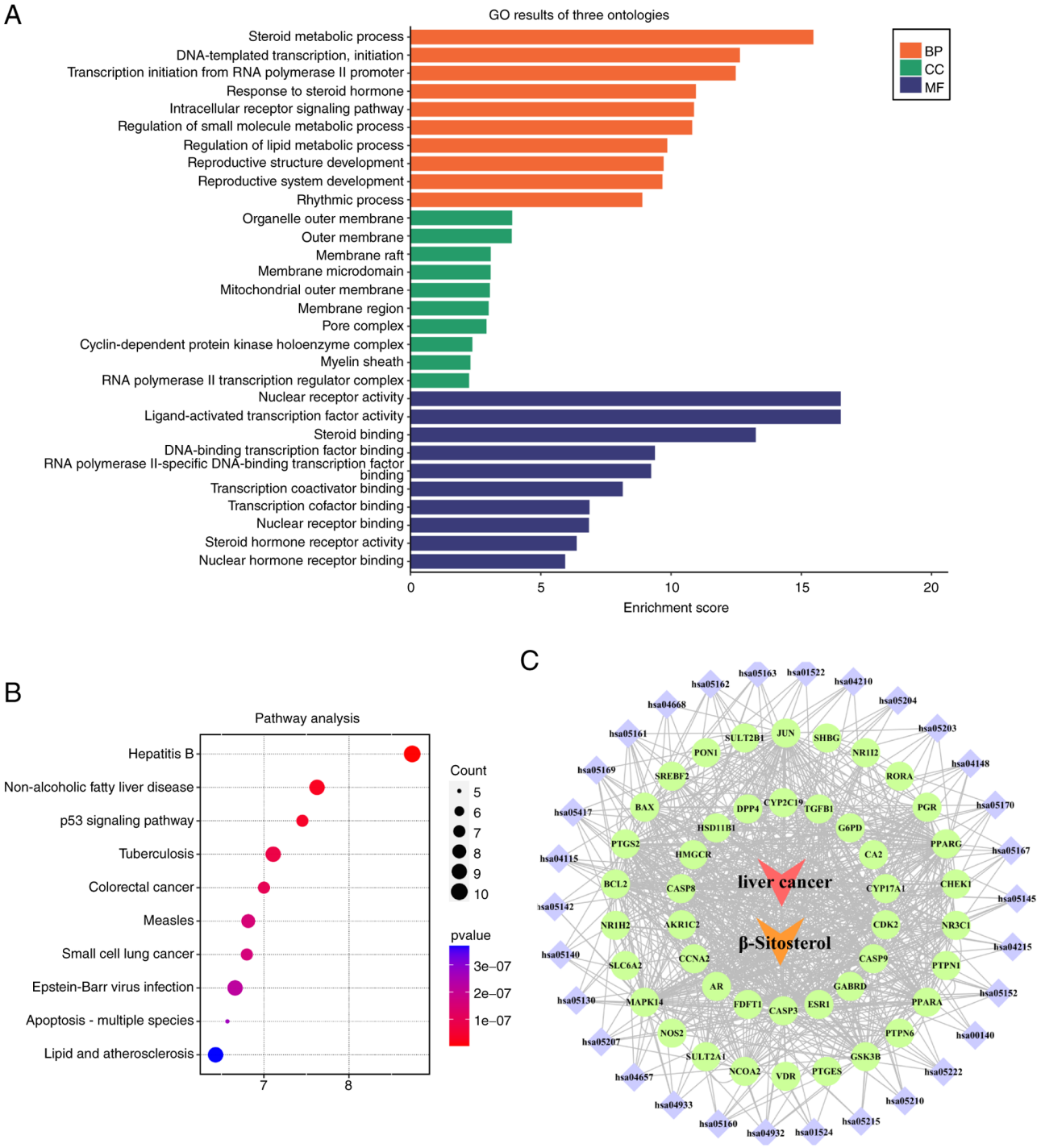


Figure 8. Enrichment analysis results and interaction network of core targets. (A) Bar graph of the top 10 GO enrichment terms for the core targets. (B) Bubble chart of KEGG pathway enrichment. (C) Drug-disease-target-pathway interaction network. BP, biological processes; CC, cellular components; GO, Gene Ontology; KEGG, Kyoto Encyclopedia of Genes and Genomes; MF, molecular functions.

these data suggest that BS may exhibit antimetastatic activity against HepG2 cells.

BS inhibits the expression of liver cancer-associated proteins MMP-2 and MMP-9. Western blot analysis and immunofluorescence showed that BS dose-dependently reduced MMP-2 and MMP-9, two metastasis-related proteins, in HepG2 cells. The levels of the loading control, GAPDH, was largely unchanged (Fig. 12A and B). Quantification confirmed a significant reduction in expression of both proteins after BS treatment. These results suggest that BS may reduce the invasive and migratory potential of liver cancer cells.

BS promotes p53 signaling pathway-induced apoptosis in HepG2 cells. KEGG pathway analysis highlighted the p53 signaling pathway as a key pathway. CCK-8 assay results indicated that HepG2 cells treated with 20 μM PFT-α or DMSO for 24 h showed no significant inhibition of cell viability (Fig. 13A). Therefore, 20 μM was used as the working concentration for PFT-α. TUNEL staining results (Fig. 13B)

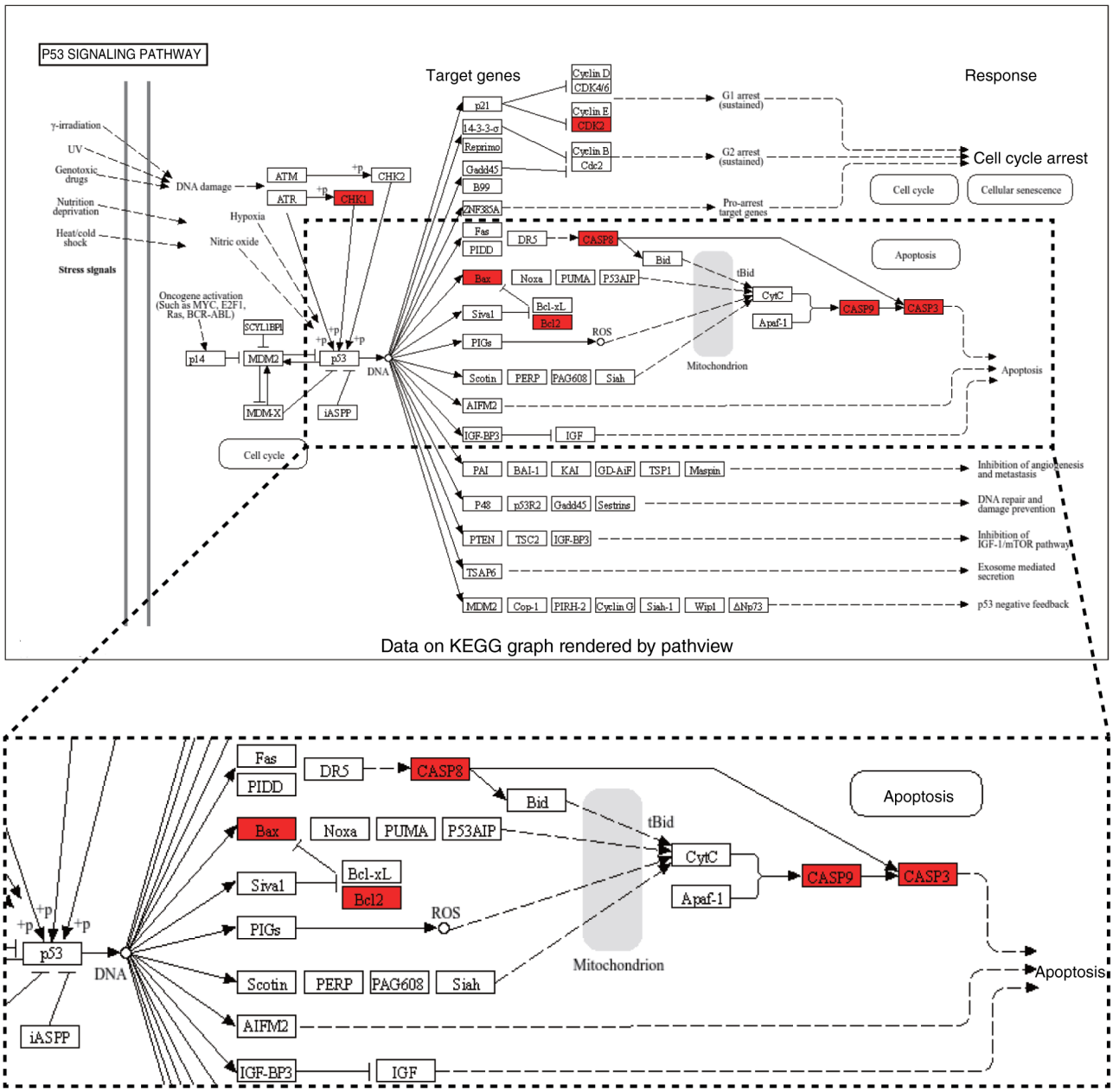


Figure 9. Schematic of the p53 signaling pathway, with potential targets for BS highlighted in red. BS, β-sitosterol; KEGG, Kyoto Encyclopedia of Genes and Genomes.

showed that BS alone significantly induced apoptosis, while co-treatment with PFT-α partly reversed this effect, suggesting that p53 pathway activation is an important, but not exclusive, mechanism for BS-induced apoptosis. In line with this, Western blot analysis and immunofluorescence showed that BS treatment alone upregulated the apoptotic regulator p53 and the downstream effector proteins cleaved caspase-3 and Bax, and downregulated the anti-apoptotic protein Bcl-2. Notably, these BS-induced changes in protein expression were significantly reversed after co-treatment with PFT-α (Figs. 13C and 14).

Discussion

To clarify the anti-liver cancer role of AS and its main bioactive constituent BS, an approach combining network prediction, molecular simulation and experimental validation was used. The data clarified their inhibitory effects and related molecular mechanisms. The results demonstrated the broad inhibitory activity of AS on the proliferation, migration and invasive capacity of HepG2 cells. Based on these results, the current study used a multilevel 'component-target-pathway' analysis to clarify the central role of BS and to outline its mechanism of promoting tumor-cell apoptosis through the p53 signaling pathway.

The therapeutic effects of TCM formulas or single herbs often reflect the combined actions of multiple active components (22). In the present study, the overall effect of AS was evaluated and then focused on its key active compound. Network pharmacology analysis suggested that AS acts on liver cancer through 67 putative targets, with enriched pathways covering multiple signaling networks related to tumor progression, including apoptosis, inflammation and

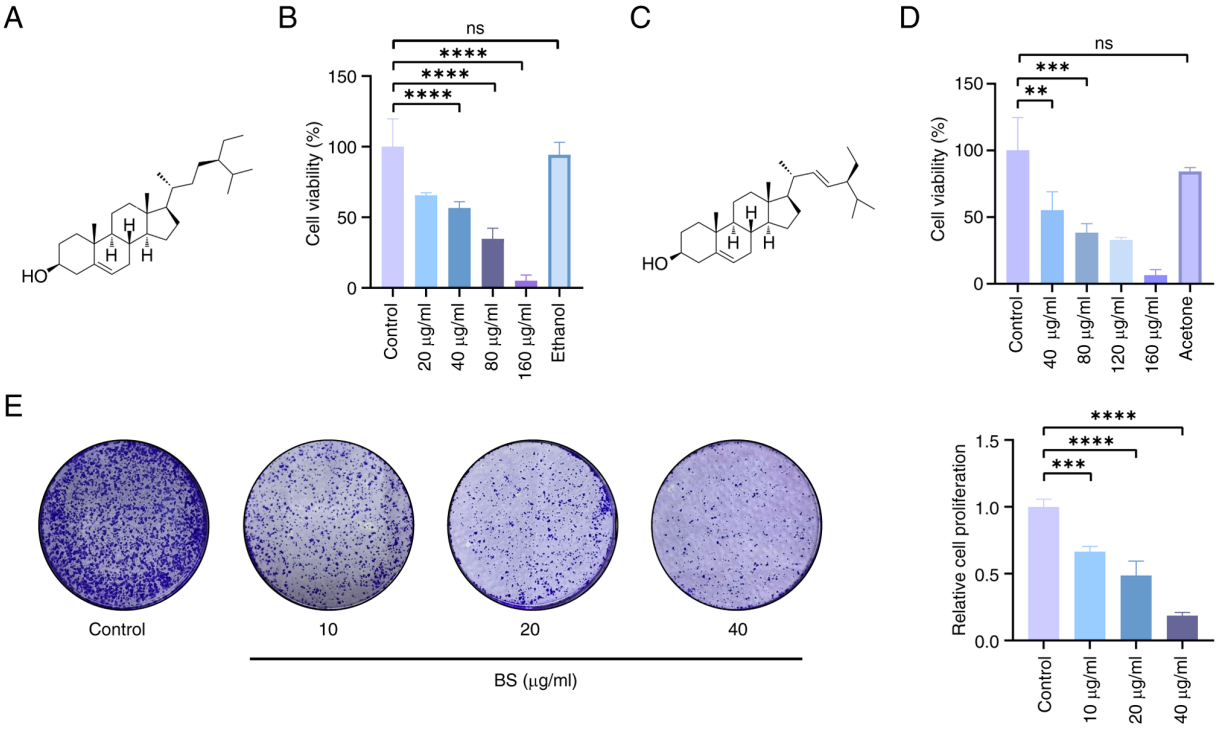


Figure 10. Comparison of the inhibitory activities of BS and ST on the viability of HepG2 cells. (A) Molecular structure of BS. (B) Effect of BS treatment on HepG2 cell viability. (C) Molecular structure of ST. (D) Effect of ST treatment on HepG2 cell viability. (E) Inhibitory effect of BS on the proliferation of HepG2 cells assessed by clonogenic assay. **P<0.01, ***P<0.001 and ****P<0.0001. BS, β-sitosterol; ns, not significant; ST, Stigmasterol.

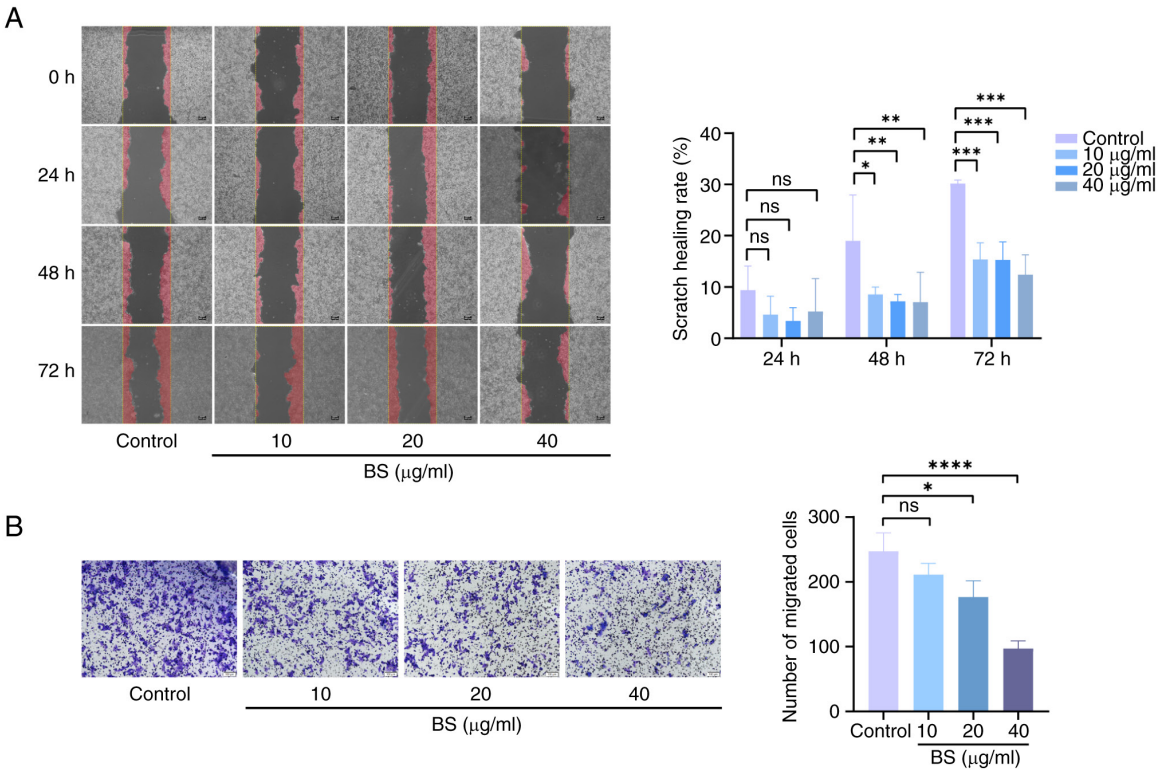


Figure 11. BS inhibited the migration of HepG2 cells. (A) BS inhibited the horizontal migration of HepG2 cells in wound healing assay, (magnification, x4; scale bar, 200 μm). (B) In Transwell experiment, BS inhibited the vertical migration of HepG2 cells, magnification, x10, scale bar, 100 μm. *P<0.05, **P<0.01, ***P<0.001 and ****P<0.0001. BS, β-sitosterol; ns, not significant.

metabolism. This is consistent with the known diverse pharmacological activities of AS, including immunomodulatory, anti-inflammatory and metabolism-related effects (23-28), suggesting that AS may exert antitumor effects by reshaping the

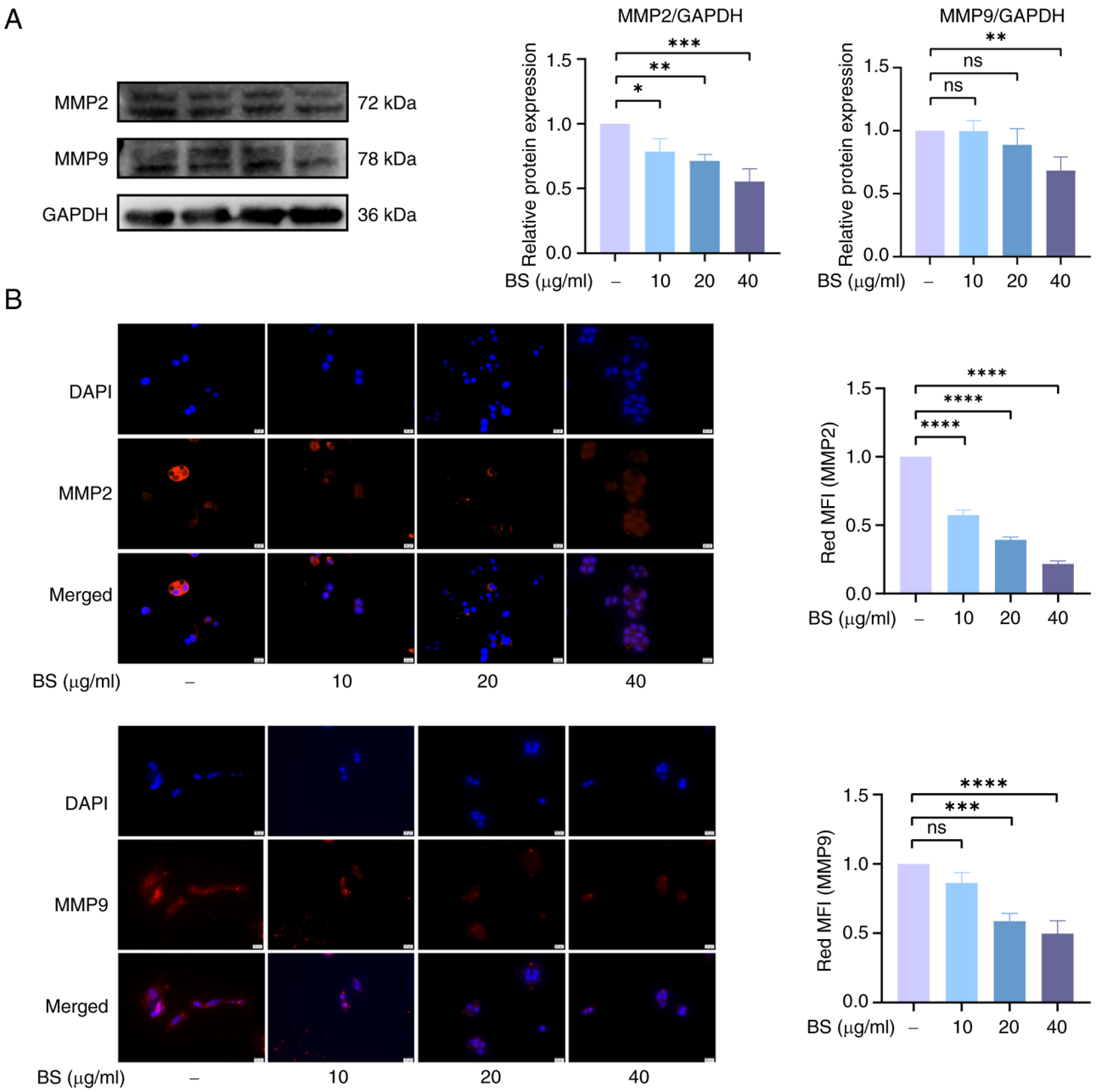


Figure 12. BS inhibits the expression of metastasis-associated proteins MMP-2 and MMP-9. (A) Western blot analysis of MMP-2 and MMP-9. (B) Immunofluorescence analysis of MMP-2 and MMP-9 protein expression, (magnification: x40; scale bar, 20 μm). *P<0.05, **P<0.01, ***P<0.001 and ****P<0.0001. BS, β-sitosterol; MFI, mean fluorescence intensity; ns, not significant.

liver cancer microenvironment in a multitarget, multipathway manner. *In vitro* validation demonstrated that AS exerted clear inhibitory effects on the viability, proliferation and migration of HepG2 cells, accompanied by reduced expression of key invasion-associated proteins, thus providing experimental support for its anti-liver cancer efficacy.

After confirming this overall effect, the bioactive constituents of AS were examined. On the basis of the aforementioned evidence for AS's multi-target anti-liver cancer effects, the present study focused on identifying the key pharmacodynamic component of AS. Through screening in the TCMSP database and evaluation that combined binding affinity, stability and cytotoxicity validation, BS was identified as a key active component of AS against liver cancer. Molecular docking revealed that BS had more stable binding with central targets, including PPARG, NFKB1 and ESR1. MD simulations further supported this finding by showing stable structures and sustained interactions in the BS-target complexes. Cell assays also showed that the inhibitory activity of BS against HepG2 cell proliferation (IC_{50}=41.19 μg/ml) was superior to that of another candidate component, ST (IC_{50}=50.93 μg/ml). This route from 'herbal whole to component screening to identification of key monomer', fits a common paradigm in the modernization of TCM research.

However, it should be noted that establishing the central role of BS does not exclude the contributions of other components in AS. Indeed, AS is rich in several components with reported antitumor activities, such as ferulic acid,

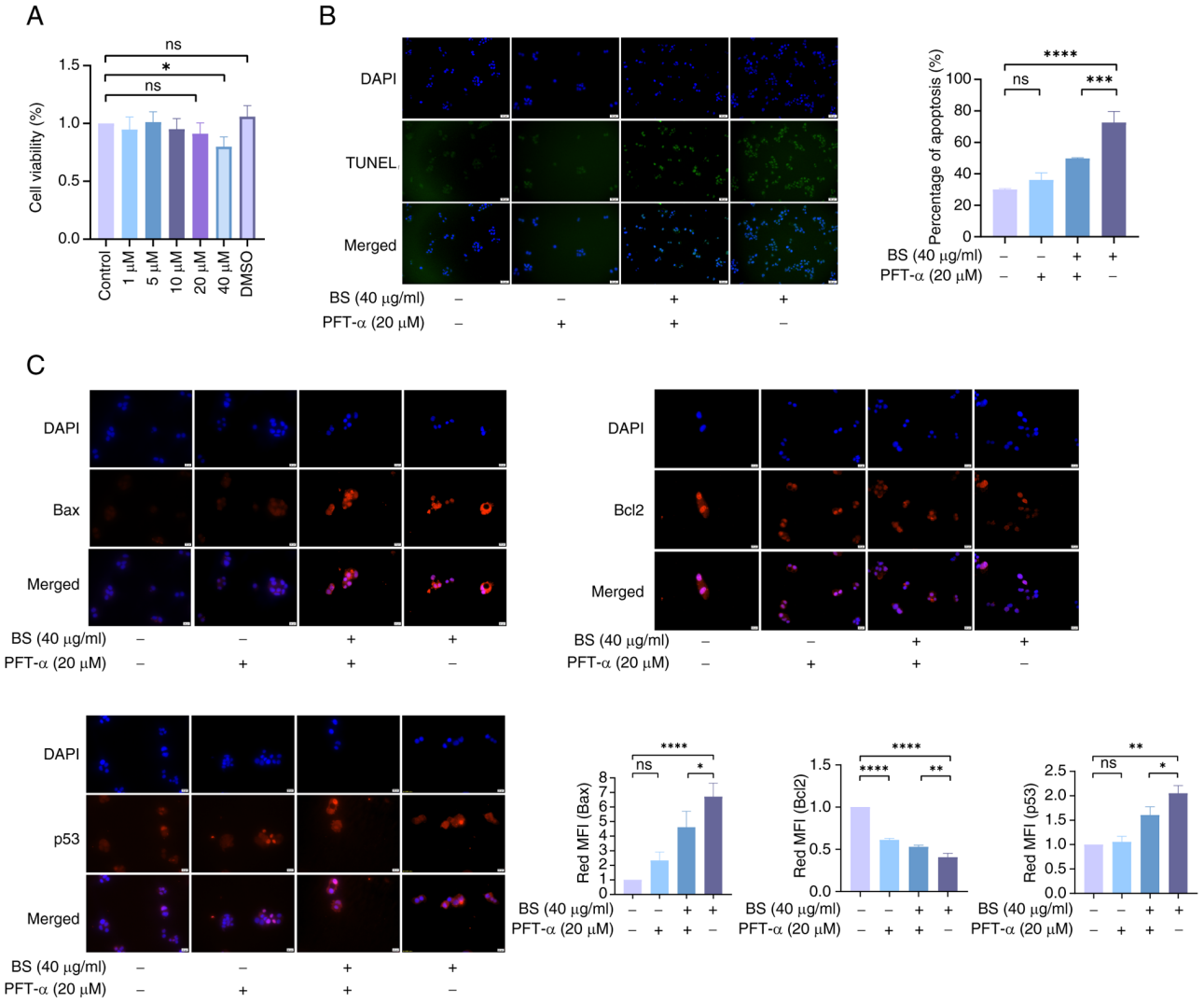


Figure 13. BS induces apoptosis in HepG2 cells via the p53 signaling pathway. (A) Effect of PFT-α (a specific p53 inhibitor) on HepG2 cell viability assessed by CCK-8 assay. (B) Effect of BS on apoptosis in HepG2 cells detected by TUNEL assay, (magnification, x20; scale bar, 50 μm). (C) Immunofluorescence analysis of the expression of apoptosis-related proteins Bax and Bcl-2, and the pathway protein p53, (magnification x40; scale bar, 20 μm). *P<0.05, **P<0.01, ***P<0.001 and ****P<0.0001. BS, β-sitosterol; CCK, Cell Counting Kit; MFI, mean fluorescence intensity; ns, not significant; PFT- α, Pifithrin-α hydrobromide.

ligustilide and Angelica polysaccharides (29). For example, ferulic acid may act by inhibiting the NF-κB pathway, ligustilide can modulate the PI3K/Akt pathway to trigger apoptosis, and Angelica polysaccharides can modulate the MAPK pathway to inhibit growth (30-32). Although these components act through different upstream pathways, their downstream effects, such as inhibiting proliferation and inducing apoptosis, largely overlap with the ultimate effects observed for BS in the present study. This suggests that the anti-liver cancer activity of AS likely results from a 'multi-component, multipathway, multitarget; synergistic effect. Different components may act on different key nodes in tumor development, leading to additive or complementary effects, thus forming the overall pharmacodynamic network. Therefore, BS can be viewed as a critical and active 'node' within this network, but not the sole active substance. Future work should use combinatorial pharmacology and orthogonal experimental design to systematically analyze the interactions among various active components, to clarify the holistic mechanism of action of AS.

After identifying the key role of BS, the present study also moved from cellular phenotypes to mechanism. Network pharmacology predictions highlighted the p53 signaling pathway as a core pathway potentially regulated by BS. The crucial tumor suppressor gene and central regulator of cellular stress responses, p53, controls key processes including cell cycle arrest, DNA repair, apoptosis and inhibition of angiogenesis (33-36). It is frequently mutated or functionally silenced in liver cancer and this is associated with tumor progression, metastasis, and therapy resistance.

The *in vitro* experimental results of the present study supported these predictions. At the phenotype level, BS significantly inhibited the colony formation and migration of HepG2 cells dose-dependently. At the protein level, this treatment was accompanied by downregulated MMP-2 and MMP-9 protein expression. Because MMPs are key effectors of tumor invasion and metastasis, and their transcription is negatively regulated by the p53 pathway (37,38), the migration inhibition and MMP downregulation phenotypes induced by BS, together suggest that its antimetastatic effect may involve activation of the p53

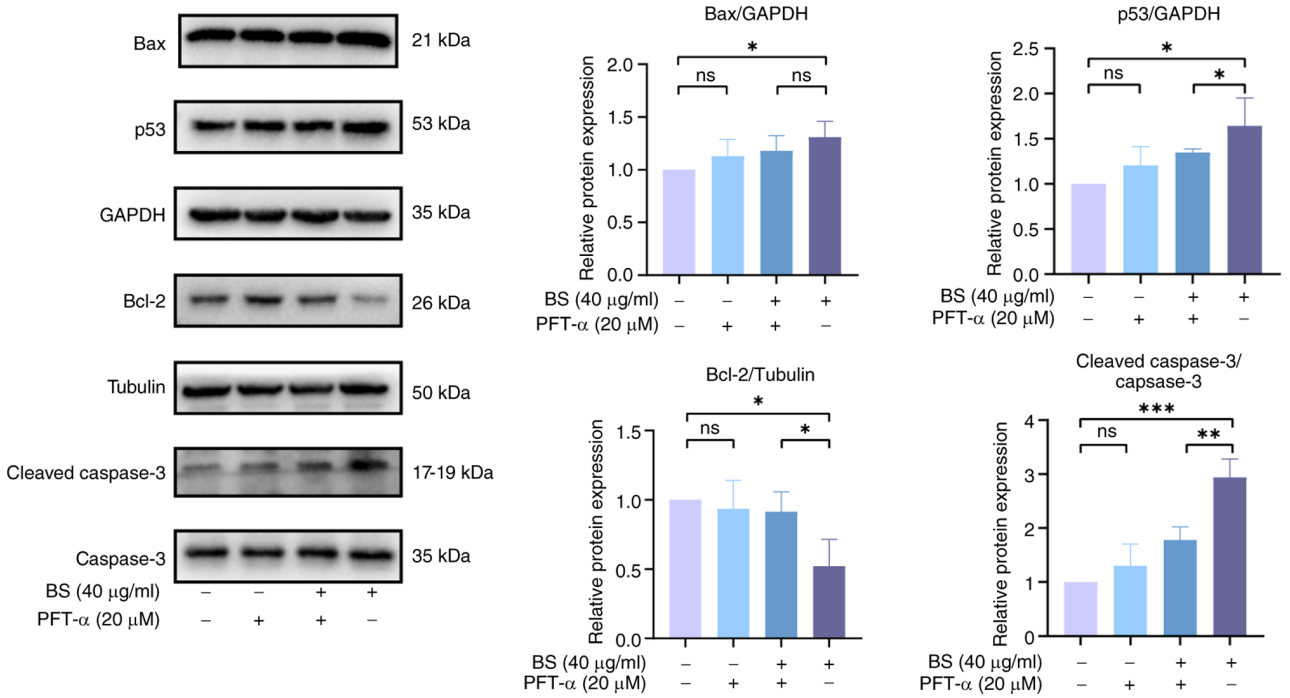


Figure 14. Western blot analysis of target proteins. Western blot analysis of Bax, Bcl-2, cleaved caspase-3 and p53 protein levels. *P<0.05, **P<0.01 and ***P<0.001. BS, β-sitosterol; ns, not significant; PFT-α, Pifithrin-α hydrobromide.

pathway, thus suppressing MMP expression. This provides an initial functional link between BS and the p53 pathway.

Subsequently, apoptosis assays gave more direct mechanistic evidence. TUNEL staining showed that BS significantly induced apoptosis in HepG2 cells. Western blot analysis and immunofluorescence analyses also revealed that BS treatment produced a clear apoptosis-related expression pattern, with increased levels of p53 and Bax proteins and reduced Bcl-2 expression, and activated the apoptosis executioner protein cleaved caspase-3. These molecular events outline a possible pathway for BS-induced apoptosis: BS may activate p53, alter the balance of Bcl-2 family proteins (increasing the Bax/Bcl-2 ratio) and activate caspase-3 to drive apoptosis. This p53-mediated mitochondrial apoptosis pathway is one of the main mechanisms of intrinsic apoptosis (39-43). The findings in the current study extend reports by Chen *et al* (44) on BS inhibiting HepG2 cell proliferation via other pathways, collectively revealing the multi-mechanistic anti-liver cancer properties of BS. The data in the current study are also consistent with reports of BS promoting apoptosis in other tumor types, such as colon, breast and pancreatic cancers (45-47).

In summary, by combining computational prediction with experimental validation, the present study revealed a direct mechanism of BS against liver cancer: Regulating the Bax/Bcl-2 balance and inducing cell apoptosis through the p53 signaling pathway. This provides a molecular-level explanation for the anti-liver cancer activity of BS and offers useful clues for research into the active material basis and mechanism of action of AS against liver cancer.

Although these findings are informative, several limitations should be noted. First, although this study focused on BS and confirmed its important role, it did not fully elucidate the complex network of multi-component synergy within AS, a common challenge in studies of the overall effects of TCM. Second, the present study used only *in vitro* models. This is an important limitation because it limits its translational value. The *in vivo* environment involves multiple factors, including pharmacokinetics, tissue distribution and the tumor microenvironment (for example immune infiltration and angiogenesis) (48), which cannot be fully reproduced *in vitro*. In the absence of *in vivo* studies using mouse xenograft models for liver cancer, the findings from the current study, although meaningful, remain preliminary and their potential clinical relevance needs direct validation. Therefore, future studies should assess the effects of AS and BS on histopathology and molecular biomarkers *in vivo*. Third, this study only used the HepG2 cell line, and the lack of validation in other liver cancer cell models (for example Huh7 and MHCC97-H) limits the general applicability of the conclusions.

To address these gaps, future work should prioritize the following directions. First, the range of liver cancer cell lines should be expanded (for example, incorporating Huh7 and MHCC97-H) to verify the consistency of the findings across different cellular contexts and enhance the reliability of the conclusions. Second, and most importantly, establishment of liver cancer mouse xenograft models (subcutaneous or orthotopic) would allow systematic evaluation of the *in vivo* antitumor activity and safety of AS and BS, thus providing critical pharmacodynamic evidence. Third, integrating multiomics approaches such as serum pharmacochemistry, metabolomics and proteomics to define the metabolic transformation of AS and BS *in vivo* and their systemic regulatory effects at both the whole-organism level and the tumor microenvironment. Fourth, testing combinations of other active components of AS with BS to better reconstruct the overall activity pattern of AS. Ultimately, where feasible, conducting

relevant clinical observational studies to investigate the potential of BS or AS-related components as adjuvant therapeutic agents or efficacy biomarkers for liver cancer, to better support translation.

In conclusion, present study explored how AS and BS act against liver cancer by combining network pharmacology with cellular experiments. The results from the current study demonstrated that AS may act through multiple targets and pathways. In particular, BS suppressed the proliferation of HepG2 cells and promoted apoptosis through the p53 pathway. Overall, this work provides a clearer basis for future exploration of the clinical use and mechanisms of AS and BS in liver cancer therapy.

Acknowledgements

Not applicable.

Funding

This study was supported by the following funds: i) Sichuan Science and Technology Education Joint Fund (grant no. 2024NSFSC2016); ii) Sichuan Provincial Administration of Traditional Chinese Medicine (grant no. 2024MS146); iii) Sichuan Clinical Research Center for Geriatric Medicine (grant no. 23LHPDZZD06); iv) Sichuan Collaborative Innovation Center for Elderly Care and Elderly Health (grant no. 23LHNBZZD08); v) Clinical Scientific Research Fund of Chengdu Medical College and Affiliated Hospital of Sichuan Nursing Vocational College (Sichuan Third People's Hospital; grant no. 24LHXHZW1-03); and vi) Postgraduate Research Innovation Fund of Chengdu Medical College in 2024 (grant no. YCX2024-01-06).

Availability of data and materials

The data generated in the present study may be requested from the corresponding author.

Authors' contributions

YD and YS confirm the authenticity of all the raw data. YD, YS and YF were involved in the conceptualization, methodology, formal analysis, investigation, data curation and writing of the original draft. Specifically, they performed the majority of the experimental work, including cell culture, molecular biology experiments and data collection and analysis. YD, YS and YF also took the lead in drafting the manuscript and preparing the figures and tables. WL, YZ and HS provided critical feedback on the experimental design and data interpretation. WL, YZ and HS assisted in the visualization of data and the preparation of figures. BT and JW were involved in the conceptualization, data analysis and interpretation and project administration of the study, as well as providing valuable insights and suggestions. LC and FD supervised the entire study, secured the funding and were involved in the conceptualization, project administration and the writing, reviewing, and editing of the manuscript. LC and FD provided overall guidance and ensured the integrity of the research. All authors read and approved the final version of the manuscript.

Ethics approval and consent to participate

Not applicable.

Patient consent for publication

Not applicable.

Competing interests

The authors declare that they have no competing interests.

References

1. Hu X, Wei J, Liu P, Zheng Q, Zhang Y, Zhang Q, Yao J and Ni J: Organoid as a promising tool for primary liver cancer research: A comprehensive review. Cell Biosci 14: 107, 2024.
2. Chan YT, Zhang C, Wu J, Lu P, Xu L, Yuan H, Feng Y, Chen ZS and Wang N: Biomarkers for diagnosis and therapeutic options in hepatocellular carcinoma. Mol Cancer 23: 189, 2024.
3. Bray F, Laversanne M, Sung H, Ferlay J, Siegel RL, Soerjomataram I and Jemal A: Global cancer statistics 2022: GLOBOCAN estimates of incidence and mortality worldwide for 36 cancers in 185 countries. CA Cancer J Clin 74: 229-263, 2024.
4. Zhu L, Meng Q, Qian W, Shao W, Lu Y, Jin S, Zhang A, Yan SG and Lu J: LARP3 inhibits the apoptosis of hepatocellular carcinoma via the ROS/PI3K/c-Fos axis. PLoS One 20: e0317454, 2025.
5. Chen JG, Zhang YH, Lu JH and Kensler TW: Liver cancer etiology: Old issues and new perspectives. Curr Oncol Rep 26: 1452-1468, 2024.
6. Lu Q, Kou D, Lou S, Ashrafizadeh M, Aref AR, Canadas I, Tian Y, Niu X, Wang Y, Torabian P, *et al*: Nanoparticles in tumor microenvironment remodeling and cancer immunotherapy. J Hematol Oncol 17: 16, 2024.
7. Anwanwan D, Singh SK, Singh S, Saikam V and Singh R: Challenges in liver cancer and possible treatment approaches. Biochim Biophys Acta Rev Cancer 1873: 188314, 2020.
8. Ji G, Li Y, Zhang Z, Li H and Sun P: Recent advances of novel targeted drug delivery systems based on natural medicine monomers against hepatocellular carcinoma. Heliyon 10: e24667, 2024.
9. Wu J, Tang G, Cheng CS, Yeerken R, Chan YT, Fu Z, Zheng YC, Feng Y and Wang N: Traditional Chinese medicine for the treatment of cancers of hepatobiliary system: From clinical evidence to drug discovery. Mol Cancer 23: 218, 2024.
10. Xu Q, Bauer R, Hendry BM, Fan TP, Zhao Z, Duez P, Simmonds MS, Witt CM, Lu A, Robinson N, *et al*: The quest for modernisation of traditional Chinese medicine. BMC Complement Altern Med 13: 132, 2013.
11. Chao WW and Lin BF: Bioactivities of major constituents isolated from *Angelica sinensis* (Danggui). Chin Med 6: 29, 2011.
12. Zhang K, Liu W, Shen F, Luan G, Han Y, Xu J, Fu C, Wu W, Hou Y, Jiang M, *et al*: Ligustilide covalently binds to Cys703 in the pre-S1 helix of TRPA1, blocking the opening of channel and relieving pain in rats with acute soft tissue injury. J Ethnopharmacol 330: 118217, 2024.
13. Liu C, Li J, Meng FY, Liang SX, Deng R, Li CK, Pong NH, Lau CP, Cheng SW, Ye JY, *et al*: Polysaccharides from the root of *Angelica sinensis* promotes hematopoiesis and thrombopoiesis through the PI3K/AKT pathway. BMC Complement Altern Med 10: 79, 2010.
14. Alvarez-Sala A, Attanzio A, Tesoriere L, Garcia-Llatas G, Barberá R and Cilla A: Apoptotic effect of a phytosterol-ingredient and its main phytosterol (β-sitosterol) in human cancer cell lines. Int J Food Sci Nutr 70: 323-334, 2019.
15. Wei WL, Zeng R, Gu CM, Qu Y and Huang LF: *Angelica sinensis* in China-A review of botanical profile, ethnopharmacology, phytochemistry and chemical analysis. J Ethnopharmacol 190: 116-141, 2016.
16. Liu C, Wu Y, Wang Y, Yang F, Ren L, Wu H and Yu Y: Integrating 16 S rRNA gene sequencing and metabolomics analysis to reveal the mechanism of *Angelica sinensis* oil in alleviating ulcerative colitis in mice. J Pharm Biomed Anal 249: 116367, 2024.

17. Ru J, Li P, Wang J, Zhou W, Li B, Huang C, Li P, Guo Z, Tao W, Yang Y, *et al*: TCMSP: A database of systems pharmacology for drug discovery from herbal medicines. J Cheminform 6: 13, 2014.
18. Hou T, Wang J, Li Y and Wang W: Assessing the performance of the MM/PBSA and MM/GBSA methods. 1. The accuracy of binding free energy calculations based on molecular dynamics simulations. J Chem Inf Model 51: 69-82, 2011.
19. Bassiouni W, Ali MAM and Schulz R: Multifunctional intracellular matrix metalloproteinases: Implications in disease. FEBS J 288: 7162-7182, 2021.
20. Cabral-Pacheco GA, Garza-Veloz I, Castruita-De la Rosa C, Ramirez-Acuña JM, Perez-Romero BA, Guerrero-Rodriguez JF, Martinez-Avila N and Martinez-Fierro ML: The roles of matrix metalloproteinases and their inhibitors in human diseases. Int J Mol Sci 21: 9739, 2020.
21. Meng XY, Zhang HX, Mezei M and Cui M: Molecular docking: A powerful approach for structure-based drug discovery. Curr Comput Aided Drug Des 7: 146-157, 2011.
22. Li S, Zhang B, Jiang D, Wei Y and Zhang N: Herb network construction and co-module analysis for uncovering the combination rule of traditional Chinese herbal formulae. BMC bioinformatics 11 (Suppl 11): S6, 2010.
23. Niu X, Zhang J, Ni J, Wang R, Zhang W, Sun S, Peng Y, Bai M and Zhang Z: Network pharmacology-based identification of major component of *Angelica sinensis* and its action mechanism for the treatment of acute myocardial infarction. Biosci Rep 38: BSR20180519, 2018.
24. Liu W, Li Z, Feng C, Hu S, Yang X, Xiao K, Nong Q, Xiao Q, Wu K, Li XQ and Cao W: The structures of two polysaccharides from *Angelica sinensis* and their effects on hepatic insulin resistance through blocking RAGE. Carbohydr Polym 280: 119001, 2022.
25. Kuang X, Wang LF, Yu L, Li YJ, Wang YN, He Q, Chen C and Du JR: Ligustilide ameliorates neuroinflammation and brain injury in focal cerebral ischemia/reperfusion rats: Involvement of inhibition of TLR4/peroxiredoxin 6 signaling. Free Radic Biol Med 71: 165-175, 2014.
26. Yang F, Lin ZW, Huang TY, Chen TT, Cui J, Li MY and Hua YQ: Ligustilide, a major bioactive component of *Angelica sinensis*, promotes bone formation via the GPR30/EGFR pathway. Sci Rep 9: 6991, 2019.
27. Shen J, Zhang M, Zhang K, Qin Y, Liu M, Liang S, Chen D and Peng M: Effect of Angelica polysaccharide on mouse myeloid-derived suppressor cells. Front Immunol 13: 989230, 2022.
28. Caturano A, Erul E, Nilo R, Nilo D, Russo V, Rinaldi L, Acierno C, Akkus E, Koudelkova K, Cerini F, *et al*: Metabolic dysfunction-associated steatotic liver disease, insulin resistance and hepatocellular carcinoma: A deadly triad. Eur J Clin Invest 56: e70132, 2026.
29. Sun Y, Guo R, Geng Y, Shang H, Guo X, Wu Y, Wang Y, Li L, Li X, Zhang S, *et al*: Longitudinal distribution map of the active components and endophytic fungi in *Angelica sinensis* (Oliv.) diels root and their potential correlations. Metabolites 14: 48, 2024.
30. Wang T, Gong X, Jiang R, Li H, Du W and Kuang G: Ferulic acid inhibits proliferation and promotes apoptosis via blockage of PI3K/Akt pathway in osteosarcoma cell. Am J Transl Res 8: 968-980, 2016.
31. Wu Y, Rong L, Zhang S, He Y, Song N, Zuo G and Mei Z: Ligustilide inhibits the PI3K/AKT signalling pathway and suppresses cholangiocarcinoma cell proliferation, migration, and invasion. Recent Pat Anticancer Drug Discov 20: 200-212, 2025.
32. Ren C, Luo Y, Li X, Ma L, Wang C, Zhi X, Zhao X and Li Y: Pharmacological action of *Angelica sinensis* polysaccharides: A review. Front Pharmacol 15: 1510976, 2025.
33. Jiang L, Zhang Q, Ren H, Ma S, Lu C, Liu B, Liu J, Liang J, Li M and Zhu R: Dihydromyricetin enhances the chemo-sensitivity of nedaplatin via regulation of the p53/Bcl-2 pathway in hepatocellular carcinoma cells. PLoS One 10: e0124994, 2015.
34. Engeland K: Cell cycle regulation: p53-p21-RB signaling. Cell Death Differ 29: 946-960, 2022.
35. Janic A, Abad E and Amelio I: Decoding p53 tumor suppression: A crosstalk between genomic stability and epigenetic control? Cell Death Differ 32: 1-8, 2025.
36. Rana JN, Mumtaz S, Choi EH and Han I: ROS production in response to high-power microwave pulses induces p53 activation and DNA damage in brain cells: Radiosensitivity and biological dosimetry evaluation. Front Cell Dev Biol 11: 1067861, 2023.
37. Wang Y, Zhang YX, Kong CZ, Zhang Z and Zhu YY: Loss of P53 facilitates invasion and metastasis of prostate cancer cells. Mol Cell Biochem 384: 121-127, 2013.
38. Song Y, Du Y, Li W, Fan Y, Zhang Y, Shen H, Cheng L, Wang J, Deng F and Tang B: Targeting the p38/MAPK pathway to induce apoptosis: A multidimensional mechanistic exploration of Mentha and its active compound diosmetin against liver cancer. Sci Rep 15: 39432, 2025.
39. Oropesa Ávila M, Fernández Vega A, Garrido Maraver J, Villanueva Paz M, De Lavera I, De La Mata M, Cordero MD, Alcocer Gómez E, Delgado Pavón A, Álvarez Córdoba M, *et al*: Emerging roles of apoptotic microtubules during the execution phase of apoptosis. Cytoskeleton (Hoboken) 72: 435-446, 2015.
40. Huang L, Xu K, Yang Q, Ding Z, Shao Z and Li E: ANXA2 in cancer: Aberrant regulation of tumour cell apoptosis and its immune interactions. Cell Death Discov 11: 174, 2025.
41. Hastak K, Gupta S, Ahmad N, Agarwal MK, Agarwal ML and Mukhtar H: Role of p53 and NF-kappaB in epigallocatechin-3-gallate-induced apoptosis of LNCaP cells. Oncogene 22: 4851-4859, 2003.
42. Carneiro BA and El-Deiry WS: Targeting apoptosis in cancer therapy. Nat Rev Clin Oncol 17: 395-417, 2020.
43. Estaquier J, Vallette F, Vayssiere JL and Mignotte B: The mitochondrial pathways of apoptosis. Adv Exp Med Biol 942: 157-183, 2012.
44. Chen Y, Yang Y, Wang N, Liu R, Wu Q, Pei H and Li W: β-Sitosterol suppresses hepatocellular carcinoma growth and metastasis via FOXM1-regulated Wnt/β-catenin pathway. J Cell Mol Med 28: e18072, 2024.
45. Baskar AA, Ignacimuthu S, Paulraj GM and Al Numair KS: Chemopreventive potential of beta-Sitosterol in experimental colon cancer model-an in vitro and in vivo study. BMC Complement Altern Med 10: 24, 2010.
46. Awad AB, Roy R and Fink CS: Beta-sitosterol, a plant sterol, induces apoptosis and activates key caspases in MDA-MB-231 human breast cancer cells. Oncol Rep 10: 497-500, 2003.
47. Cao ZQ, Wang XX, Lu L, Xu JW, Li XB, Zhang GR, Ma ZJ, Shi AC, Wang Y and Song YJ: β-Sitosterol and gemcitabine exhibit synergistic anti-pancreatic cancer activity by modulating apoptosis and inhibiting epithelial-mesenchymal transition by deactivating Akt/GSK-3β signaling. Front Pharmacol 9: 1525, 2019.
48. Bruni D, Angell HK and Galon J: The immune contexture and Immunoscore in cancer prognosis and therapeutic efficacy. Nat Rev Cancer 20: 662-680, 2020.

Copyright © 2026 Du et al. This work is licensed under a Creative Commons Attribution-NonCommercial-NoDerivatives 4.0 International (CC BY-NC-ND 4.0) License.